JOURNAL OF GEOPHYSICAL RESEARCH, VOL. 107, NO. C8, 3105. 10.1029/2000JC000760, 2002

Coherent Doppler Profiler measurements of near-bed suspended sediment fluxes and the influence of bed forms

C. Smyth and Alex E. Hay
Department of Oceanography, Dalhousie University, Halifax, Nova Scotia, Canada

L. Zedel
Department of Physics and Physical Oceanography, Memorial University of Newfoundland, St. John's, Newfoundland, Canada

Received 8 December 2000; revised 3 January 2002; accepted 15 January 2002; published 14 August 2002.

[1] This paper reports on remote acoustic observations of vertical turbulence intensity and vertical suspended sediment flux profiles on a planar beach in 3–4 m water depth. The measurements of suspended sediment concentration and velocity are colocated and simultaneous and extend through the wave bottom boundary layer to the bed with 0.7 cm vertical resolution. Normalized cospectra of the suspended sediment flux and the vertical velocity for different bed states (irregular ripples, cross ripples, linear transition ripples, and flat bed) indicate a small but significant peak at incident wave frequencies but are otherwise rather flat, with weak redness. Estimates of the vertical flux components indicate a general balance between upward fluxes due to waves and turbulence and downward settling. Two exceptions to this balance are found immediately above the bed and for nonmigrating irregular ripples. The contribution from the high-frequency turbulent component is small. Wave phase averages for low-energy bed states exhibit near-bed peaks in the suspended sediment flux following wave phase reversal. Wave phase averages for the high-energy cases do not exhibit a diffusive signature. Observed vertical profiles of turbulence intensity for different bed states reveal that the near-bed turbulence levels are relatively independent of bed state. Friction velocity predictions from presently available models, including a bed stress model and a sediment eddy diffusion model, are compared to measured values of near-bed turbulence intensity. Reasonable agreement is found between measured and predicted bottom friction velocities when wave friction factors from *Tolman* [1994] are used. *INDEX TERMS:* 4568 Oceanography: Physical: Turbulence, diffusion, and mixing processes; 4546 Oceanography: Physical: Nearshore processes; 4558 Oceanography: Physical: Sediment transport; *KEYWORDS:* Coherent Doppler Profiler, nearshore processes, turbulent boundary layer, suspended sediment fluxes, bedforms, wave friction factor

1. Introduction

[2] In the nearshore zone, waves and turbulence entrain and suspend seafloor sediments, creating clouds of sediment-laden fluid near the seafloor. The presence of suspended sediment may be highly intermittent, with patches of sediment-laden fluid detectable infrequently in the water column. Alternatively, sediment puffs can be quasi-periodic, with ripple crests shedding vortices of sediment-laden fluid into the water column every half-wave cycle. In both cases, turbulence and vortical flow over bed roughness elements are responsible for the suspended sediment clouds and sediment flux away from the bed. In natural conditions, mobile sediments at the bed adopt different geometric configurations, or bed states, as a function of wave forcing energetics. A quantitative description of suspended sediment fluxes for the observed range of bed states is lacking, in part because there are few field measurements of near-bed turbulence and suspended sediment fluxes.

[3] Observations of the seafloor indicate a variety of bed states that have distinctive geometries and length scales [*Clifton*, 1976]. Recently, *Hay and Wilson* [1994] have shown, using acoustic sensors to record bed state images, that Clifton's progression of bed states occurs as a function of time at a fixed location during storm evolution. Figure 1 shows example images of these bed state, taken from the present study.

[4] Since a variety of bed states exists with different length scales, heights, and crest geometries, it is plausible that different ripple types are associated with different mechanisms for sediment suspension and redistribution.

[5] Recent technological advances have also enabled measurements of near-bed suspended sediment flux. Figure 2 shows data obtained with a Coherent Doppler

0148-0227/02/2000JC000760$09.00

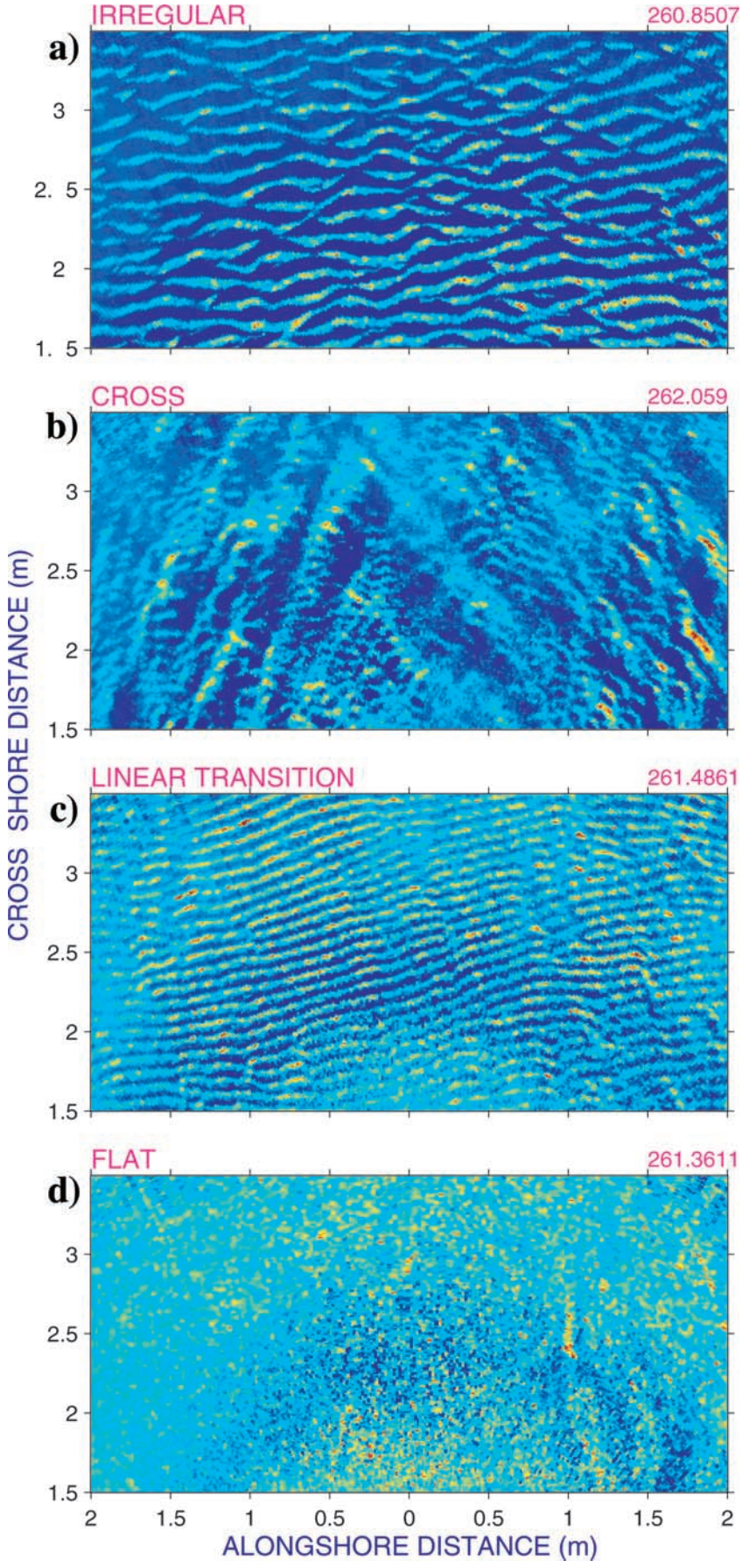
IRREGULAR
260.8507
a)
CROSS
262.059
b)
LINEAR TRANSITION
261.4861
c)
FLAT
261.3611
d)
CROSS SHORE DISTANCE (m)
ALONGSHORE DISTANCE (m)
3
2. 5
2
1. 5
2.5
1.5
2
1.5
1
0.5
0
0.5
1
1.5
2

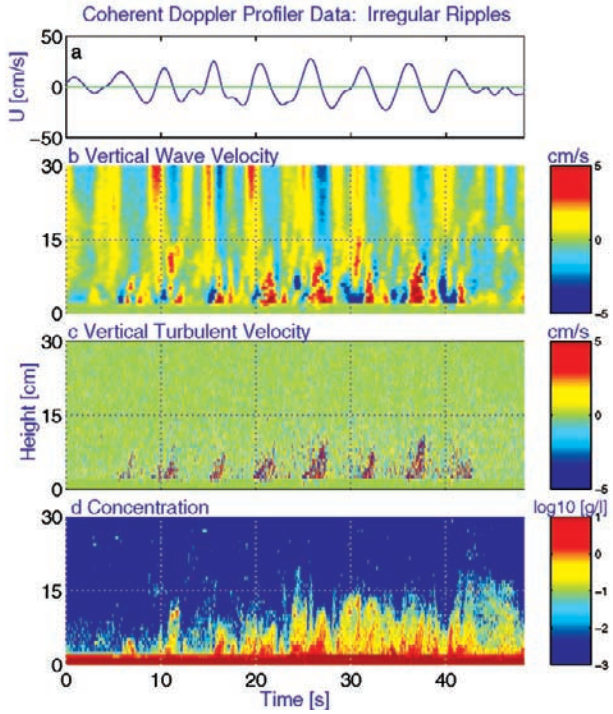

Figure 2. Coherent Doppler Profiler (CDP) data during a 45 s time interval for relatively low-energy waves over irregular ripples. (a) Horizontal orbital wave velocities at 20 cm height. (b) Vertical profiles of the low-pass filtered vertical wave velocities (<2 Hz) are shown for a 30 cm vertical range. (c) Vertical profiles of the high-pass filtered vertical velocities (> 2 Hz). (d) Vertical profiles of the logarithm of the suspended sediment concentration. The horizontal velocity, u, is positive onshore, and the vertical velocity, w, is positive upward.

Profiler (CDP) [*Zedel and Hay*, 1999]: high resolution vertical profiles of velocity and suspended sediment concentration are obtained simultaneously at the same points in a vertical profile, enabling direct estimates of the suspended sediment flux.

[6] A central objective of this study is to compare near-bed measurements of suspended sediment fluxes and turbulence intensity for the observed bed states. There are two primary goals. One is to test the assumption often made in sediment suspension models [e.g., *Glenn and Grant*, 1987], of a balance in the vertical between the vertical turbulent flux and the gravitational settling flux. The second is to investigate the relationship between near-bed turbulence intensity and bottom friction. The approach is first to partition the velocity into wave and turbulent components, then to investigate the vertical structure of ensemble and wave phase averaged turbulence intensity and suspended sediment fluxes for different bed states.

[7] A second objective is to compare the observations for different bed states to laboratory observations of turbulence and sediment suspension under waves. Laboratory observations indicate that the process of suspending and distributing sediments can be either diffusive or convective. The distinction between diffusion and vortex shedding is based on the mixing length relative to the overall scale of the suspended sediment concentration profile [*Nielsen*, 1992, p. 233]: a diffusive process has a small relative mixing length while a convective process has a large relative mixing length. As the term "convective" is often associated with buoyancy-driven flow, it will not be used in this paper, and is instead replaced with the term "vortex shedding process". Observations by *Jensen et al.* [1989] of diffusive boundary layer growth over smooth and sandpaper beds in a U-shaped oscillatory flow water tunnel showed that during the decelerating phase of the wave, bed-generated turbulence diffused continuously away from the bed and was almost uniformly distributed with depth in the wave boundary layer by the time free stream reversal occurred. Observations by *Nakato et al.* [1977] of vortex shedding in a U-shaped oscillatory tunnel over a rippled bed showed that prominent peaks in suspended sediment concentration and turbulence intensity during the wave cycle were associated with sediment-laden vortices that formed in the lee of each ripple during each half period. At wave reversal, the vortex expanded and moved away from the ripple, carrying fluid with high concentrations of suspended sediment upward into the interior flow. Laboratory observations of vortex shedding by *Sleath* [1987] over fixed sand and pebble beds showed that the upward propagation velocity of the maximum turbulence intensity was constant with height over 1–2 boundary layer thicknesses. *Nielsen* [1992, p. 236] suggests that the upward propagation velocity for ripple shed vortices would be quantitatively similar.

[8] Three presently available models that predict the average near-bed turbulence intensity are here compared to measured turbulence levels. These models do not specify the bed state directly, but may use bed form dimensions in roughness parameterizations. The first model, a bed stress model, typically assumes that friction velocity squared is given by the wave energy multiplied by a wave friction factor. The available parameterizations for the wave friction factor are based primarily on laboratory measurements and are not well known for mobile sediments and the variety of bed states encountered in field conditions [*Nielsen*, 1992; *Tolman*, 1994]. The second model considered for near-bed turbulence is a vortex shedding model by *Sleath* [1991] which predicts the turbulence intensity profile based on a grid-stirring model. The hypothesis is that the turbulence produced by oscillatory flow over bottom roughness is similar to turbulence produced by an oscillating grid *Sleath*

Figure 1. (opposite) Acoustic images of (a) irregular ripples, (b) cross ripples, (c) linear transition ripples, and (d) flat bed during the experiment. The time stamp, in year day, is indicated in the upper right-hand corner. Each image is a 2 m × 4 m rectangular section in the offshore portion of a larger circular (5 m radius) ensonified region. The fan beam is located at the origin. The offshore direction is toward increasing negative cross-shore distance. Lighter colors represent regions of strong return, delineating ripple slopes that are facing the rotating transducer. The large dark arc is an artifact of the transducer beam pattern. Data were collected using a rotary fan beam sonar from *Hay et al.* [1999].

[1991]. Finally, the third selected model is a diffusion model, which predicts the turbulence intensity based on a sediment eddy diffusivity. There are many such models. The version used here is similar to that of *Wiberg and Smith* [1983].

[9] The next section briefly describes the theory and formulation of the models considered here, followed in section 3 by a description of the field experiment site and the instrumentation. Observations of the near-bed turbulence intensity using several methods of velocity decomposition are presented in section 4. Observations of vertical suspended sediment fluxes are presented in section 5, followed by wave phase averages of vertical turbulence intensity, suspended sediment concentration, and vertical sediment fluxes in section 6. Model predictions and comparison to measurements are found in section 7.

2. Theory and Model Formulations

[10] The three models selected from the literature to compare predicted near-bed turbulence intensities to those observed in the field are a bed stress model [*Jonsson*, 1966], a sediment eddy diffusion model [*Wiberg and Smith*, 1983; *Dyer and Soulsby*, 1988], and a vortex shedding model [*Sleath*, 1991]. These models do not predict the vertical turbulence intensity directly, but instead predict the friction velocity, a turbulent velocity scale.

2.1. Bed Stress Model

[11] The simplified equation of motion for flow in the $x-z$ plane is given by

$$\rho\frac{\partial u}{\partial t} = -\frac{\partial p}{\partial x} + \frac{\partial \tau}{\partial z} \tag{1}$$

where u is the horizontal velocity, ρ is the fluid density, p is the pressure and τ is the shear stress. As in the usual boundary layer approximation the pressure gradient is assumed to be independent of z, giving in the boundary layer:

$$\rho\frac{\partial}{\partial t}(u - u_\infty) = \frac{\partial \tau}{\partial z} \tag{2}$$

where u_∞ is the free stream velocity [*Jensen et al.*, 1989]. The bed stress model defines the maximum bed shear stress during a wave cycle, τ_0, as

$$\tau_0 = \rho u_*^2 \tag{3}$$

where u_* is the friction velocity. *Jonsson* [1966] defined the bed shear stress in terms of a wave friction factor, f_w:

$$\tau_0 = \frac{1}{2}\rho f_w (A\omega)^2 \tag{4}$$

where A is the wave semiexcursion distance and ω is the wave angular frequency.

[12] Several different parameterizations for f_w have been suggested. Two are used here. The first, by *Tolman* [1994] (based on the work by *Grant and Madsen* [1982], *Wilson* [1989], and *Madsen et al.* [1990]) is

$$f_w = 0.08[\mathrm{Ker}^2 2\sqrt{\zeta_0} + \mathrm{Kei}^2 2\sqrt{\zeta_0}]^{-1} \tag{5a}$$

$$\zeta_0 = \frac{1}{21.2\kappa\sqrt{f_w}}\frac{k_N}{2A} \tag{5b}$$

where Ker and Kei are Kelvin functions of the zeroth order, κ is the von Kàrmàn constant and k_N is the wave-induced ripple roughness which includes empirically derived parameterizations for the ripple roughness at low wave energy and for sheet flow roughness at high wave energy (Section 7).

[13] The second expression for the friction factor is from *Swart* [1974]:

$$f_w = \exp[5.213\left(\frac{r}{A}\right)^{.194} - 5.977] \tag{6}$$

where r is the bed roughness. The bed roughness may be taken as a grain roughness ($r \sim d_{50}$) or may be estimated as the equivalent bed roughness. The latter quantity can be estimated from [*Nielsen*, 1992, p. 158]:

$$r = \frac{8\eta^2}{\lambda} + 170\sqrt{\theta_{2.5} - 0.05}D \tag{7}$$

where η is the bed form height, λ is the wavelength, D is the grain diameter, and $\theta_{2.5}$ is the grain roughness Shields parameter [*Nielsen*, 1992, p. 105] defined by

$$\theta_{2.5} = \frac{1}{2}f_{2.5}\psi \tag{8}$$

The addition of the grain roughness Shields parameter term takes into account the roughness contribution from moving sand grains. In the above equation $f_{2.5}$ is the grain roughness friction factor based on equation (6) with r set to 2.5 times the median grain diameter, d_{50}. The mobility number, ψ is given by

$$\psi = \frac{A^2\omega^2}{(s-1)gd_{50}} \tag{9}$$

where ω is the wave angular frequency, s is the ratio of the particle to fluid density, and g is acceleration due to gravity.

[14] The semiexcursion distance, A is taken as $2u_{rms}/\omega$ for irregular waves, using a significant wave orbital velocity of $2u_{rms}$ [*Thornton and Guza*, 1983], and ω is the peak angular frequency. Measurements of bed roughness, wave RMS velocity, and wave period will be used to estimate the friction velocity from the bed stress model using equations (3)–(5) for comparison to the measured vertical turbulence intensity. The ratio of the friction velocity to the peak vertical turbulence intensity is between 1 and 2, based on previous laboratory studies by van Doorn (in [*Nielsen*, 1992, p. 72]) and *Sleath* [1987] of oscillatory flow over fixed roughness elements.

2.2. Sediment Eddy Diffusion Model

[15] The sediment eddy diffusion model is based on an assumed balance between settling of particles and an

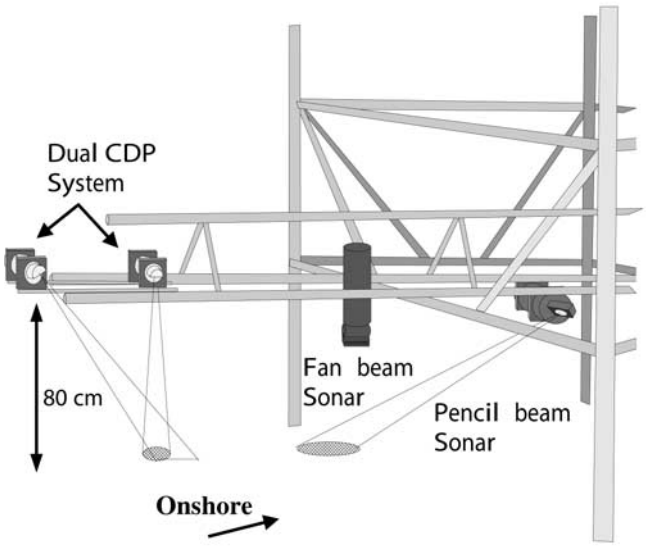

Figure 3. Schematic showing the instrument positions on the mast. The dual-CDP system was approximately 80 cm above the bed. Located adjacent to the CDPs were a rotary fan beam sonar and a pencil beam sonar. Only three of the four bottom-piercing vertical support pipes are shown.

upward diffusion of particles away from the bed due to turbulence, plus an additional vertical flux due to the vertical component of wave motion

$$\bar{c}\,\overline{w} + \overline{\tilde{c}\tilde{w}} + \overline{c'w'} = 0, \tag{10}$$

where w is the vertical velocity, c is the suspended sediment concentration, an overbar represents the time average over the entire data run, a tilde the wave component, and a prime the fluctuating component. The turbulent sediment flux is parameterized by a sediment eddy diffusivity, K, times a mean concentration gradient:

$$\overline{c'w'} = -K\frac{d\bar{c}}{dz}, \tag{11}$$

where z is the height above the bed. The sediment eddy diffusivity near the bed is assumed to have the same form as the momentum eddy viscosity [*Smith*, 1977; *Grant and Madsen*, 1979]:

$$K = \kappa u_* z \tag{12}$$

where $\kappa = 0.4$ is the von Kàrmàn constant, although the the ratio of these two quantities has been found to vary from 0.1 to 10 [*Dyer and Soulsby*, 1988]. Other forms of the eddy viscosity have been suggested [*Sleath*, 1990, p. 270]. *Nielsen* [1992, p. 236] argues that a sediment eddy diffusion model does not contain the important contribution to the vertical suspended sediment fluxes from vortex shedding. Thus it is interesting to study the sediment eddy diffusion model for the irregular ripples, for which vortex shedding is expected to be a significant process.

[16] The suspended sediment concentration was separated into mean and fluctuating components, $c = \bar{c} + \hat{c}$. Separating the fluctuating component into wave and turbulent components was not attempted to avoid difficulties in filtering a highly intermittent, positive definite quantity.

[17] Thus $\overline{\hat{c}\tilde{w}}$ represents the component of the flux which is correlated with wave motions. Similarly, the turbulent suspended sediment flux is $\overline{\hat{c}w'}$.

[18] Using the above decompositions, the sediment eddy diffusivity is estimated from

$$K = \left(\frac{d\bar{c}}{dz}\right)^{-1}(\bar{c}\,\overline{w} + \overline{\tilde{c}\tilde{w}}) \tag{13}$$

using CDP measurements of the average gradient of the concentration, the mean flux, and the wave flux. If K exhibits a linear region near the bed, the friction velocity can be estimated from the slope of K with height. Stratification effects due to high concentration levels may also be included, but these effects were found to be small in a nearshore experiment (in ~2 m water depth with a median grain diameter of 200 μm [*Sheng and Hay*, 1995]) and are assumed small here.

2.3. Vortex Shedding Model

[19] The vortex-shedding model developed by *Sleath* [1991] assumes that turbulent vortices shed by ripples, combine and diffuse in a similar manner to vortices produced by oscillating grids in grid-stirring experiments. By applying the parameterizations from laboratory grid stirring experiments [*Thompson and Turner*, 1975] to experiments with roughened beds in an oscillating tunnel, Sleath obtained the empirical relationship:

$$w'_{rms} = \frac{1}{b_s z}, b_s = 6.29\frac{T}{A^{3/2}k_s^{1/2}}, \tag{14}$$

where T is the wave period, A is the semiexcursion distance and k_s is the roughness of the bed.

[20] *Sleath* [1987] used fixed grain roughness beds. For mobile beds, a direct analogy to the grid stirring experiments is the ripple wavelength as the appropriate length scale, at least for two dimensional ripples. Other choices include ripple height and equivalent bed roughness [*Nielsen*, 1992, p. 158]. Using these roughness parameterizations, predictions of b_s from this model will be compared to the measured values.

3. Field Experiment Summary

[21] Data were collected over an 11 day period in the fall of 1995 near Queensland Beach, Nova Scotia, Canada. The beach is a pocket beach O(100 m) long, located in a bay which is sheltered except for a narrow entrance to the open shelf, and which the beach faces directly (see *Crawford and Hay* [2001] for details on the site geometry). Instrumentation was located approximately 80 m offshore, nominally 1 m above the bottom in 3–4 m water depth depending upon the tide. This beach lacked a bar system and had a cross-shore slope of approximately 2° at the instrument location. The sand had a median grain diameter of 175 μm.

[22] A 3-D view of the instrument support frame is shown in Figure 3. The support frame was a space frame (2 m × 1.5 m) clamped to four pipes which were jetted into

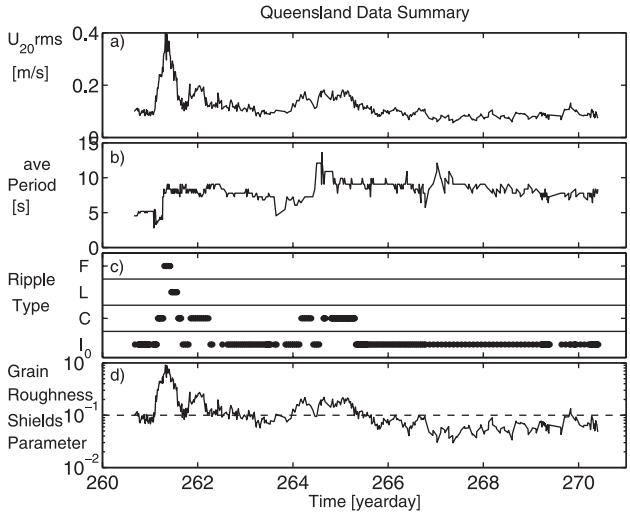

Figure 4. (a) RMS of the horizontal velocity at 20 cm off the bed for the 11 day experiment. A storm occurred early in the experiment, on year day 261 (18 September) and long period swell was observed during day 264. (b) Time series of the wave period based on the spectral maximum. (c) Ripple type: F = Flat bed, L = Linear transition ripples, C = Cross ripples, and I = Irregular ripples. (d) Grain roughness Shields parameter and the selected 0.1 threshold.

the bed. Instruments were positioned away from the support frame and bottom-piercing support pipes using a cantilevered mast. During the deployment, rotary fan beam sonar images and rotary pencil beam profiles of the seafloor provided estimates of bed form type and dimensions [*Hay and Wilson*, 1994; *Wilson and Hay*, 1995; *Ngusaru*, 2000]. Five consecutive images were collected every half hour during storm conditions and every hour during low-energy conditions. As shown in the experiment summary in Figure 4, irregular ripples were present for most of the experiment. Cross ripples were present during the spin-up and spin-down of a 1 day storm as well as during a brief interval of long-period swell. Flat bed and linear transition ripples occurred at or close to the storm maximum. Bed form conditions responded to wave forcing, showing a progression of ripples with increasing wave energy: irregular ripples, followed by cross ripples, linear transition ripples and finally flat bed. Bed form type is highly correlated with the grain roughness Shields parameter [*Wilson and Hay*, 1995]. The waves during this experiment were mainly nonbreaking [*Crawford and Hay*, 2001] except perhaps during flat bed conditions.

[23] The ripple dimensions are given in Table 1. Ripple height was taken as $2\sqrt{2}$ times the standard deviation of the filtered seafloor elevation, σ_Z. Selected filter bands (0.5–3 cpm for cross ripples, 3– 10 cpm for irregular ripples, and 10–15 cpm for linear transition ripples) were chosen based on separation of the fan beam power spectral densities at a variety of azimuthal angles [*Hay et al.*, 1999]. For sinusoidal ripples, $\eta = \eta_0 \cos lx$, the wavelength can be estimated as

$$\lambda = 2\pi \frac{|\,\eta\,|}{|\,d\eta/dx\,|}, \tag{15}$$

where l is the ripple wave number. As the irregular and cross ripple bed states are characterized by a range of scales, the wavelength was estimated as

$$\lambda = 2\pi \frac{\sigma_Z}{\sigma_{dZ/dx}}, \tag{16}$$

where $\sigma_{dZ/dx}$ is the RMS of the spatial derivative of the elevation. Note that specifying a single wavelength for highly 3-D cross ripples is a significant simplification. The wavelength estimate in this study is based on the large oblique ripples, using a cross-shore profile. This method gives a larger estimate than the wavelength taken in a sense perpendicular to the crest, but this is the scale encountered by the fluid during the wave orbital excursion. Linear transition ripples are nearly sinusoidal [*Crawford and Hay*, 2001] and the wavelength was estimated as the wavelength at the maximum of the weighted power spectral density from the fan beam data. A criterion of a grain roughness Shields parameter greater than 0.1 was applied to the irregular ripple case to remove very low wave energy conditions. This limit is close to the typical threshold of no motion of 0.05 for sand in oscillatory flow [*Nielsen*, 1992, p. 107].

[24] Coincident profiles of vertical and cross-shore velocity, and suspended sediment concentration were made using a two-beam Coherent Doppler Profiler (CDP) system [*Zedel et al.*, 1996]. The CDP system was configured to operate with 0.7 cm vertical range resolution over a 80 cm vertical range using 9 pulse pair averages. Vertical velocities are estimated to have an uncertainty of 0.5 cm/s for single pulse pair processing based on tow-tank calibrations [*Zedel et al.*, 1996] giving ±0.17 cm/s for the present data. This system has been calibrated for conversion from acoustic backscatter levels to absolute concentration and corrected for attenuation using the methods described by *Hay* [1991]. In total, 412 data files were collected, each containing approximately 7 min of data sampled at 28 Hz. The sampling routine during nonstorm conditions consisted of two data files separated by a 3 min interval, repeated each hour. During storm conditions, the repetition time interval was decreased to half an hour.

4. Mean Turbulence Intensities

[25] In this section, analysis of the profiles of vertical turbulence intensity are presented in order to better understand the role of turbulence and wave motions in suspended sediment fluxes and their relationship to bed state. The first obstacle to overcome is accurate separation the velocity into mean, $\overline{w}$, wave, $\tilde{w}$, and turbulent, w', components. There is no generally accepted method of velocity decomposition, particularly for the irregular waves and variable bed form geometries typical of nearshore field conditions. It is there-

Table 1. Average Bed Form Dimensions (±Standard Deviation) for the Queensland Experiment Based on Rotary Sonar Data[a]

Bed State	Number	η, cm	λ, cm
Irregular ripples	63	0.9 ± 0.2	17 ± 1
Cross ripples	77	2.3 ± 0.7	72 ± 19
Linear transition	14	0.33 ± 0.02	10.7 ± 0.4
Flat bed	14	0.035	–

[a] Ripple height and wavelength are given by η and λ, respectively.

fore appropriate at this stage to determine the level of consistency among different decomposition methods that have been suggested.

4.1. Velocity Decomposition

4.1.1. Filter method

[26] The filter method of decomposition uses a high-pass filter, separating the turbulent from wave velocities with a 2 Hz cutoff. This method has been used by others with similar cutoff frequencies: 0.8 Hz, *Kosyan et al.* [1996]; and 2 Hz, *Foster* [1997]. Since the cutoff frequency is higher than the incident wave peak frequency in the vertical velocity spectra, much of the incident wave band energy is removed from the turbulent velocity. This method incorporates noise and aliased energy into the turbulence regime. Aliased energy was not removed as it is assumed to be part of the turbulence. The filter was a 5th order Butterworth filter which had a magnitude response of approximately −100 dB at 0.2 Hz.

4.1.2. Linear wave theory method

[27] In the second method considered, the wave velocity is calculated using linear inviscid wave theory and removed from the velocity, thereby giving the turbulent velocity as the residual. Measured horizontal velocities at 20 cm height were used to determine the vertical wave velocity, $\tilde{w}$:

$$\tilde{w} = \frac{\tanh kz}{\omega}\frac{\partial \tilde{u}}{\partial t}, \tag{17}$$

where z is the height above bottom, $\tilde{u}$ is the low-pass filtered horizontal velocity and k is the wave number obtained from the dispersion relation

$$\omega^2 = gk\tanh kh \tag{18}$$

where g is the acceleration due to gravity, and h is the water depth. Wave velocities were estimated spectrally for wave periods between 2 and 20 s. Since this model is inviscid and assumes the bed is flat, the turbulence intensity predicted by this model is assumed to be an upper limit.

4.1.3. Dissipation rate method

[28] The third decomposition method was developed by *George et al.* [1994] for hot film measurements of surf zone turbulence, and gives an estimate of the turbulence intensity from the dissipation rate in the inertial subrange. The dissipation rate, ϵ, of a 1-D wave number spectrum, $\phi(k)$, may be found from the universal form for isotropic turbulence

$$\phi(k) = \alpha\epsilon^{2/3}k^{-5/3} \tag{19}$$

for the transverse component where k is the wave number and $\alpha = 2/3$ is the 1-D Kolmogorov constant [*Tennekes and Lumley*, 1972]. The turbulence intensity, w_ε is calculated from the rate of turbulent kinetic energy dissipation using

$$w_\epsilon = \sqrt{\int_{k_0}^{\infty}\phi(k)dk}, \tag{20}$$

which simplifies to

$$w_\epsilon = \sqrt{\frac{3\alpha}{2}}\left(\frac{\epsilon;}{k_t}\right)^{1/3}, \tag{21}$$

where k_t is defined by the turbulent length scale, $l_t = 2\pi/k_t$. For $z < 0.2h$, the turbulent length scale was set equal to the height above bed [*George et al.*, 1994], giving

$$w_\epsilon = \sqrt{\frac{3\alpha}{2}}\left(\frac{\epsilon z}{2\pi}\right)^{1/3}. \tag{22}$$

[29] In the present analysis, spectra were estimated for 1 s time windows centered on the crests of the 35 largest waves in each 7 min data set. The spectral slopes in the 0.9–10.5 Hz frequency range were used to calculate the dissipation rate using the measured horizontal advection velocity at 20 cm height, u_{20}, to convert from frequency to wave number space according to Taylor's hypothesis. Fitted slopes were required to have a minimum regression correlation coefficient of 0.6. Only time intervals of weak turbulence relative to the mean flow were used: that is, with $w_{rms}/\bar{u} < 0.2$ over the 1 s window. As well, only spectral slope estimates steeper than a threshold of −0.75 were used in the calculation of ϵ (spectral slopes are discussed in section 4.3). These restrictions eliminated approximately 80% of the data near the bed and 10–40% of the data at 50 cm above the bed. Average dissipation rates were calculated from the combined estimates of the dissipation rate for each ripple type by fitting a normal distribution to $\log(\epsilon)$ to determine the mean, μ, and variance, σ^2. The average dissipation rate was then calculated as $\exp(\mu + \sigma^2/2)$. Conversion from the average dissipation rate to turbulence intensity was accomplished using equation (22).

4.2. Turbulence Intensity Profiles

[30] Profiles of vertical RMS velocity (Figure 5) demonstrate that the three decomposition methods give similar vertical profiles. Note that two of the estimates of vertical turbulence intensity are averages over the entire time series while the dissipation rate method estimates the turbulence intensity during short time windows about the wave crests.

[31] The vertical RMS velocity, or turbulence intensity, is smallest for the dissipation rate, and largest for the linear wave theory method. Profiles for the low-energy cases are similar: intensity levels peak between 0.7 and 2 cm above the bed, falling off slowly with height. For the high-energy cases, the turbulence profiles exhibit a nearly constant level of turbulence with height, although the dissipation rate method results exhibit an increase with height. It is interesting that the irregular ripples have the highest value of near-bed turbulence, particularly since the significant orbital velocities are 3 times lower than they are for flat bed conditions. High turbulence levels for the irregular ripples are likely due to vortices shed from ripple crests, which are visible in time series of the data (Figure 2). It is possible that the turbulence intensity for high-energy conditions is underestimated because the maximum turbulence intensity may be too close to the seafloor to be detected by the CDP. Turbulence with a scale of the height of the sample volume of the sensor (0.7 cm) will be measured inaccurately. This includes turbulence inside sheet flow layers. These measurements will be compared to the estimated friction velocities from the bed stress model and the eddy diffusion model in section 7.

[32] Since the average turbulence intensity is expected to be half of the value of the intensity at the wave crest

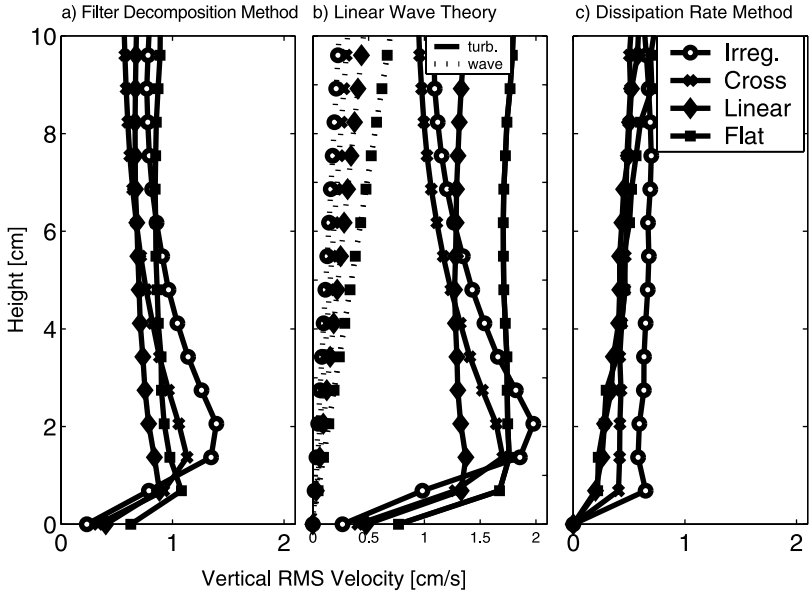

Figure 5. Measured profiles of turbulence intensity (solid) and wave intensity (dashed) are shown for the three velocity decomposition methods. (a) Filter decomposition method. (b) The same data with decomposition based on linear wave theory. (c) Friction velocity estimates from the dissipation rate method. The number of data runs for each bed state: irregular 63; cross 77; linear 14; and flat 14.

[*George et al.*, 1994], the dissipation rate method gives peak turbulence intensities which are smaller than the filter method estimates by a factor of 4–6 for the low-energy cases and 12–14 for the high-energy cases. It is difficult to reconcile these large differences, particularly for the high energy cases. The small values of the dissipation rate at high wave energies (section 4.4) suggest that the turbulent energy at large scales may be suppressed. This is because the advection velocities are largest for the flat bed, so that the dissipation rates are estimated over the lowest wave number range (largest scales) which are possibly outside the inertial subrange. It is therefore suggested that the dissipation rates are too low for the high energy cases, and in order to prevent a bias from using different wave number ranges, dissipation rates should be estimated over a fixed wave number range for all bed states with a more extensive data set.

[33] Each decomposition method yields a slightly different magnitude and vertical structure which is partly due to the nonturbulent motions. The filter method may underestimate the turbulence present as low frequency turbulent motions are excluded. In addition, the fixed cutoff frequency does not accommodate changes in high-frequency wave contribution with height. The linear wave theory method overestimates the turbulent energy as it includes motions that are related to wave motions. For example irrotational vertical motions induced by flow over bed forms [*Davies*, 1983; *Hay et al.*, 1999] are not removed by linear wave theory. As well, phase shifts in the vertical velocity are not predicted by linear wave theory and may cause small residuals in wave energy. These residuals are small compared to the wave motions, but can be large compared to the small turbulence intensities. The vertical structure of the turbulence intensity for the linear wave theory method is affected by the vertical profile of the waves which is attenuated near the bed, and by the potential flow over bed forms, which attenuates with height. Given the above limitations of each method, the actual turbulence intensity is expected to be overestimated by the linear wave theory method, and underestimated by the filter method. Since these two methods agree within a factor of 2 near the bed, these methods offer a reasonable estimate of the turbulence intensity profile.

[34] Turbulence intensities within 3 cm of the bed are higher for irregular ripples than for flat bed for either decomposition method. Assuming that turbulent boundary layer growth for irregular ripples is dominated by vortex shedding (see Figure 2) and for flat beds by diffusion, the measured turbulence intensity profiles show that higher turbulence intensities are found for a vortex shedding process. Turbulence intensities profiles for cross ripples and irregular ripples are very similar, suggesting a vortex shedding process is dominant for cross ripples. A diffusion process is expected for linear transition ripples as the profile of turbulence intensity is similar to that of the flat bed case.

4.3. Near-Bed Vertical Velocity Spectra

[35] Ensemble-averaged near-bed vertical velocity spectra for the different bed states are shown in Figure 6. Also shown for comparison is a f^{-3} slope in the orbital wave regime [*Thornton*, 1979] and the expected slope of $f^{-5/3}$ for the inertial subrange. In the orbital wave band the spectral densities are highest for flat bed, as expected, since this is the highest wave energy case. At higher frequencies, the highest spectral densities are found for the irregular ripple case, implying a significant bed form effect on the near-bed turbulence intensity. A slope break is present at about 0.4 Hz in the cross ripple and flat bed spectra, separating low-frequency orbital waves and high-frequency turbulence. This slope break is not present in the irregular ripple case.

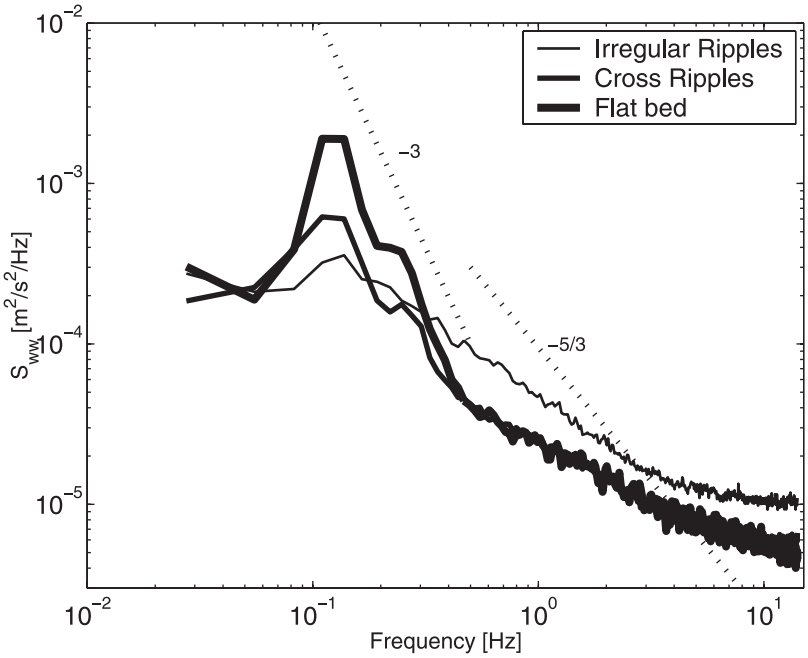

Figure 6. Ensemble-averaged vertical velocity power spectral densities, S_{ww}, at $z = 3.4$ cm for three bed states. The power spectrum for the linear transition ripple case (not shown here) closely resembles the flat bed case. Degrees of freedom for the three cases are: irregular ripples, 1386; cross ripples, 1694; and flat bed, 308.

[36] The spectral slopes for the four bed states have similar slopes above 1 Hz, and are flatter than the expected $-5/3$ slope. Close to the Nyquist frequency the spectral densities flatten out, indicating a noise floor and/or aliased energy. Aliasing can occur in the CDP because of dead time between pulse bursts [*Zedel and Hay*, 1999].

[37] In the study by *George et al.* [1994] the average slope of the spectra was found to be -1.25, flatter than the expected value of -1.67, and was thought to be caused by measurement difficulties. The average slope in this study for the near-bed 1 s windowed spectra is ~ -1, even with a threshold criterion on the spectral slope. A flatter slope than expected may explain the low turbulence intensities predicted by the dissipation rate method. At 50 cm height, the spectral slopes are closer to the expected value of -1.67, ranging from -1.45 for low-energy to -1.63 for high-energy conditions. Flatter slopes were also found in the high-frequency range of the near-bed power spectra estimated over the entire data run (Figure 6). However, the slopes of the run-averaged spectra farther away from the bed (50 cm height) approach -1.67 for all bed states.

[38] Potential reasons for the flatter slopes observed include intermittency [*McComb*, 1990, p. 329], and anisotropy in the turbulence as the bed is approached. Flatter slopes have been observed near the boundary in unidirectional turbulent boundary layers by Klebanoff (see *Hinze* [1975, p. 652]) and in turbulent oscillatory boundary layers by *Hino et al.* [1983]. This issue is beyond the scope of this paper and is being pursued in a separate study with a more extensive data set.

4.4. Dissipation Rate Estimates

[39] Average dissipation rate estimates give near-bed peak values of 9.3, 1.4, 0.1, and 0.1 cm^2/s^3 for irregular ripples, cross ripples, linear transition ripples and flat bed, respectively. These values are smaller than nearshore measurements made by *Foster* [1997], who found dissipation rates approaching 15 cm^2/s^3 in the wave bottom boundary layer, but in 2 m water depth and under a mix of breaking and nonbreaking waves. *George et al.* [1994] observed higher Froude-scaled dissipation rates of 5×10^{-6} to 1×10^{-4} for near-bed (.05 h) measurements outside the wave boundary layer under breaking waves and bores. Froude scaling multiplies the dissipation rate estimates by u^3/l where the velocity scale, u, is taken as $\sqrt{gh}$ and the length scale is taken as the water depth, h. *Foster* [1997] observed Froude-scaled dissipation rates of up to 3.4×10^{-5}, while the peak values in the present measurements range from 1.7×10^{-7} to 1.7×10^{-5}.

5. Vertical Suspended Sediment Fluxes

5.1 Vertical Flux Balance

[40] One of the key assumptions in the sediment eddy diffusion model that has never, to our knowledge, been tested by direct measurement is the existence of a balance between upward turbulent and wave suspended sediment fluxes and downward settling (equation (10)). The spatially coincident measurements of suspended sediment concentration and particle vertical velocity obtained with the CDP enable this test to be made. The results for the experiment are shown in Figure 7. There is indeed a general balance between downward settling and upward suspended sediment fluxes due to waves and turbulence. Using the filter method of velocity decomposition the turbulent suspended sediment fluxes are generally much smaller than the wave suspended sediment fluxes. However, if the linear wave theory method of velocity decomposition is used, the

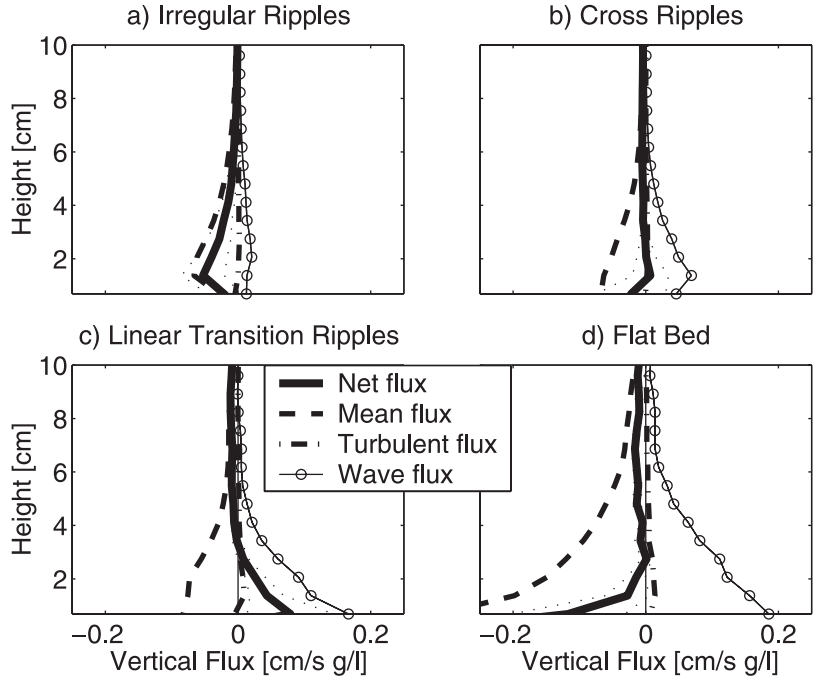

Figure 7. Measured values of vertical suspended sediment fluxes for different bed states. The net flux is the sum of the three components of the flux: the mean flux, $\bar{w}\,\bar{c}$, the wave flux, $\overline{\tilde{c}\tilde{w}}$ and the turbulent flux, $\overline{\tilde{c}w'}$. The turbulent velocity is defined by the filter method. Dotted lines about the net flux indicate the standard error about the mean. Numbers of data runs: irregular: 63; cross 77; linear 14; and flat bed 14.

upward suspended sediment fluxes are instead dominated by the turbulent component. These observations suggest a significant contribution to the flux is from large-scale eddies. Upward suspended sediment fluxes are highest near the bed, with the highest suspended sediment fluxes observed for flat bed conditions.

[41] There are departures from a balance: in particular, the irregular ripple case, and at heights above the bottom less than 3 cm for the other cases. Flux measurements are sensitive to the location of the sensor relative to the ripple profile, and may be nonzero over short time averages. Ensemble averaging removes biases due to sensor position provided the ripples migrate past the sensor so that the ensemble average is equivalent to averaging over the entire ripple profile. The irregular ripples were generally stationary [*Crawford and Hay*, 2001] and therefore do not achieve a zero net flux below 4 cm. The suspended sediment fluxes near the bed are also sensitive to the method of determining the seafloor elevation from acoustic backscatter. Presently, there is no generally accepted method for determining the seafloor elevation to subcentimeter precision over the full range of sediment transport conditions and bed states. In this study, the seafloor elevation was identified by locating the position of the 50th percentile of the maximum averaged suspended sediment concentration, plus a restriction on the suspended concentration in the range bin above. The details of this choice and comparisons to other methods are discussed in Appendix A. Although the average position of the seafloor during the 7 min data run is used, the position based on ~30 s averages sometimes changed by one range bin.

[42] Changes in the time-averaged concentration over longer timescales do not account for the net flux imbalance. The flux estimated from

$$\overline{\frac{d}{dt}\int_{0.69\text{cm}}^{20\text{cm}} < c > dz} \tag{23}$$

where angle brackets indicate an average over 30 s, is less than 0.004 cm/s g/L, which is negligible compared to the flux near the bed in Figure 7. The inference to be drawn from these measurements is that the nonzero vertical flux gradient is balanced by the horizontal flux gradient.

5.2. Suspended Sediment Flux Coherence

[43] Examination of the flux coherence (normalized cross spectra) of the vertical velocity and the suspended sediment concentration (Figure 8) reveals that the coherence is low, but higher than the 95% significance level in the low-energy cases.

[44] The flux coherence has a similar shape over elevations of 2.1–4.8 cm. For the low energy cases, a 10 point moving average was applied above 0.3 Hz. Enhanced coherence is found near the wave peak frequency for all of the bed states, with the largest coherence for flat bed conditions. This result suggests that the wave period is an important timescale for suspended sediment fluxes, and that wave phase averages are a useful tool for analyzing boundary layer behavior.

[45] The coherence is weakly red, even with relatively short time windows. Above 2 Hz, the coherence remains significant for the low-energy cases even though the flux

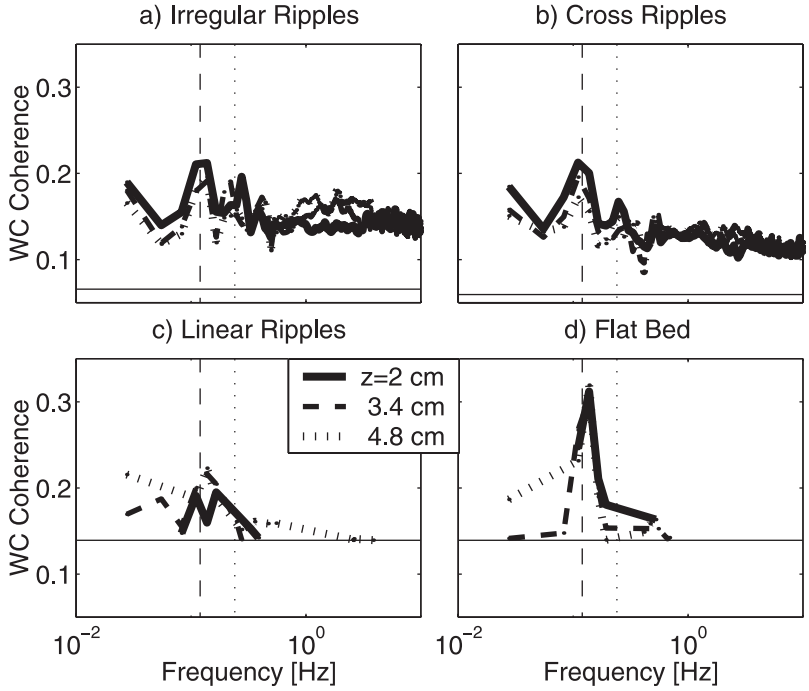

Figure 8. Coherence of the vertical flux for the four bed states. The vertical lines indicate the average incident wave peak frequency (dashed) and twice the peak frequency (dotted). Only data above the 95% significance levels are shown. A 10 point moving average was applied to the data above 0.3 Hz.

profiles (Figure 7) indicate the flux contribution from this frequency range is small. This is explained by the ensemble-averaged phase of the cross spectrum in this region (Figure 9), which above 2 Hz fluctuates between positive and negative values, implying a small contribution on average.

6. Wave Phase Averages

[46] Several authors have brought attention to the evolution of the wave bottom boundary layer over a wave period. A diffusive wave phase signature was observed in the laboratory by *Jensen et al.* [1989] who found that during the decelerating phase of the wave, bed-generated turbulence diffused continuously away from the bed and was almost uniformly distributed with depth in the wave boundary layer by the time free stream reversal was reached. A vortex shedding wave phase signature was observed by *Nakato et al.* [1977], and *Osborne and Vincent* [1996] where sediment-laden vortices expand and move away from the ripple at each wave reversal. The objective of this Section is to investigate wave phase averages of turbulence, suspended sediment concentration and suspended sediment fluxes for the different bed states and to determine if the characteristics are dominated by vortex shedding or diffusive mixing signatures. Wave phase averages were estimated for the largest 15 waves during each 7 min data run.

[47] Waves were divided into 15° phase bins based on the phase calculated from the Hilbert transform of the horizontal velocity (bandpass filtered between 0.5 and 1.5 of the peak orbital frequency). Wave phase averages of the vertical velocity components are shown in Figure 10 for the four bed states.

[48] Farther away from the bed in the low-frequency component, the maxima of the vertical velocity for irregular and cross ripples are found at 90° and 270° expected. For the high-energy cases the maxima are shifted toward 180°, the phase of the peak onshore velocity, becoming in-phase 1 cm above the bed. This vertical velocity signature is caused by the horizontal velocity flowing over a sloped bed. Although the bed slope is small (~2°), the horizontal wave velocities are large enough to induce significant vertical velocities.

[49] In the high-frequency portion of the vertical velocity (Figures 10e–10h), the wave phase averages for the ripple cases are distinct. For irregular ripples (Figure 10e), turbulence levels start to increase near the bed just before the wave crest. As the wave progresses, the high turbulence levels are found farther away from the bed, then abruptly decrease at wave phase reversal. Turbulence contours are tilted toward increasing wave phase, indicating an upward propagation away from the bed. These features are consistent with Figure 2c. For cross ripples (Figure 10f), turbulence levels have two peaks at each height associated with the wave crest and wave trough. Contour intervals are almost symmetric about the wave crest, but are slightly tilted toward decreasing wave phases. Wave phase averages for the high-energy cases (Figures 10g and 10h) are very similar and indicate turbulence enhancement at the wave crest. For these two cases, contours of the turbulence intensity are approximately symmetric about the wave crest.

[50] Wave phase averages of the suspended sediment concentration and vertical suspended sediment fluxes are shown in Figure 11. For irregular ripples (Figure 11a), enhanced suspended sediment concentrations at z = 2 cm lag the turbulence intensity maximum. Contours indicate two peaks near 4 cm height, the first near 100°, and the

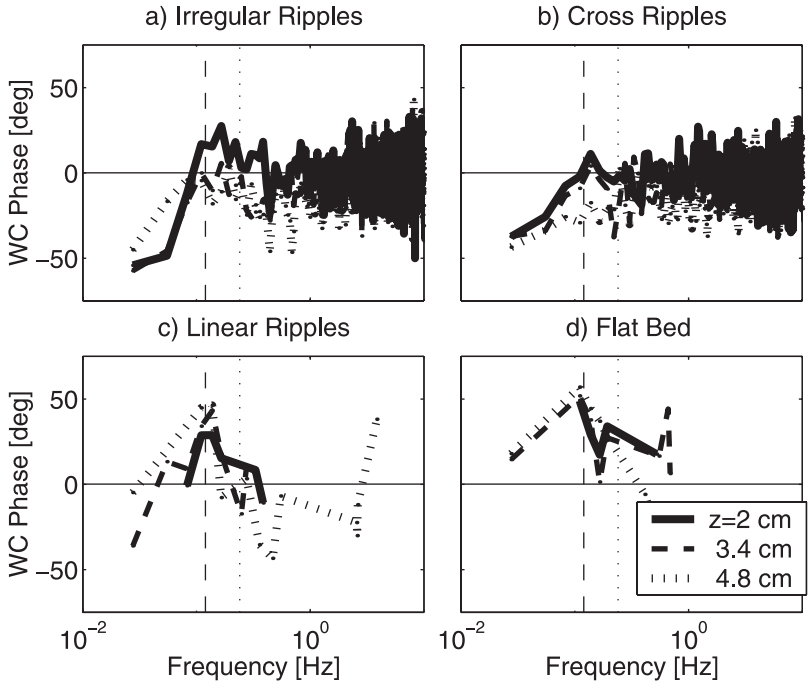

Figure 9. Phase of the vertical flux coherence for the four bed states. The vertical lines indicate the average incident wave peak frequency (dashed) and twice the peak frequency (dotted). Only data above the 95% significance levels are shown.

second near 300°. Wave phase averages for the cross ripples (Figure 11b) have a relatively constant level of suspended sediments with only a slight enhancement near 100°. The suspended sediment concentration contours are approximately constant with wave phase for the high-energy cases (Figures 11c–11d).

[51] Figures 11e –11h contains the wave phase averages of the wave suspended sediment flux component. This quantity is estimated as the time average of the product of the suspended sediment concentration fluctuation ($\hat{c} = c - \bar{c}$) and the low-pass filtered vertical wave velocity, $\tilde{w}$. For irregular ripples (Figure 11e), at 2 cm height there are two peaks in the upward fluxes. The first peak occurs just after wave phase reversal and is likely associated with the release of a vortex directly offshore of the sensor. The second peak occurs after the wave crest and propagates away from the bed, matching wave phase signatures of the suspended sediment concentration. The second peak is likely associated with the arrival of vortices from neighboring ripples. Upward fluxes for cross ripples (Figure 11f) are positive during the wave trough, propagating away from the bed, with an abrupt termination just after the zero crossing (90°). This signature, combined with a small peak in the suspended sediment concentration and the asymmetry in the turbulence intensity contours, suggests the release of a vortex directly offshore of the sensor. These signatures are much less obvious than for the irregular ripples, but the cross ripples migrated past the sensor, changing the arrival phase of the shed vortices. The absence of any signatures during the wave crest suggests that shed vortices from neighboring ripples are not being advected past the sensor. For high-energy conditions, upward suspended sediment fluxes are observed predominately at the wave crest, consistent with the turbulence maxima, but inconsistent with the concentration signatures. As the velocity near the bed is dominated by the horizontal velocity, the suspended sediment fluxes are also strongly affected by the horizontal suspended sediment fluxes.

[52] The wave phase signature of the turbulence for the irregular ripple case indicates upward propagation during the latter half of the wave crest. By determining the phase of the maximum turbulence intensity at various heights, the upward propagation velocity may be estimated for the overall wave-phase average and compared to laboratory results [*Sleath*, 1987]:

$$w_{vs} = 0.44\omega\delta_{0.05}, \tag{24}$$

where $\delta_{0.05}$ is the thickness of the boundary layer defined by the height at which the amplitude of the defect velocity is 5%, and ω is the wave angular frequency. The upward diffusion velocity for the oscillatory tunnel data of [*Jensen et al.*, 1989, Figure 34] is $0.42\omega\delta$ based on the estimated boundary layer thickness.

[53] For the field data, the boundary layer thickness was estimated from $\delta = u_*/\omega$, assuming a friction velocity of $u_* = 2w'_{1/3} = 6.1$ cm/s (filter method), and determining ω from the peak wave period. The upward propagation velocity is calculated to be $0.37\omega\delta$ as shown in Figure 12. The upward propagation velocity may also be calculated based on the phase of the maximum suspended sediment concentration. The upward propagation velocity of the concentration is $0.46\ \omega\delta$, slightly larger than the turbulent upward propagation velocity, and shows a $\sim$30° lag at the bed which diminishes with height. Thus, the propagation velocities estimated for the irregular ripple case are similar to the upward propagation velocities measured in the laboratory for fixed grain roughness.

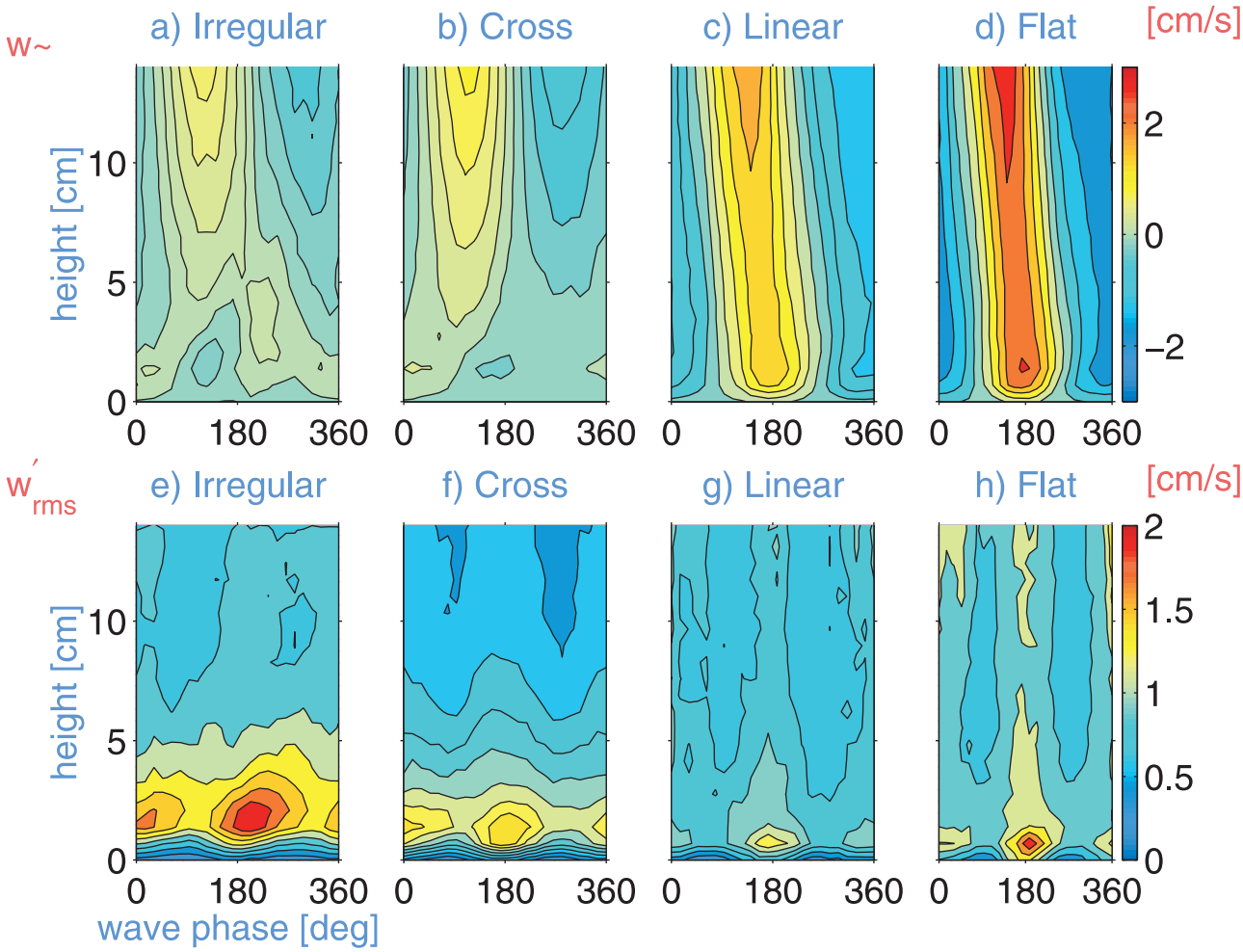

Figure 10. (a)–(d) Wave phase averages of the RMS of the low-pass filtered vertical velocity for the four bed states as a function of height and wave phase. (e)–(h) Wave phase averages of the RMS of the high-pass filtered vertical velocity, also as a function of height and wave phase. Each plot is a function of height from 0 to 14 cm, and wave phase from 0 to 360° with the peak of the onshore velocity at 180°. Number of data runs: irregular 63, cross 77, linear 12, and flat 14; 15 largest waves per data run.

[54] Data included in the calculation of the propagation velocity are indicated by filled symbols. Above the boundary layer thickness, the phase of the maximum suspended sediment concentration decouples from the near-bed phase relationship, as previously observed by *Osborne and Vincent* [1996]. The propagation velocity was estimated from a linear fit applied to the near-bed region where the phase of the maximum increases with height. Restrictions were applied to the data to prevent interference from small random noise peaks at each height. For the turbulence intensity, data between 150° and 360° were included in the fit if the peak turbulence intensity was larger than the RMS of the turbulence intensity (estimated over 360°) at each height. For the suspended sediment concentration, data were included in the fit if the maximum suspended sediment concentration was larger than 1.1 times the exponential of the mean of the logarithmic suspended sediment concentration.

[55] The upward propagation velocity of the turbulence intensity is based on the filter method, which excludes some of the large eddy turbulence. It is therefore not surprising that the measured upward propagation velocities over irregular vortex ripples are similar to laboratory diffusion results over roughened beds. The high frequency turbulence is likely generated in two ways. One is through a cascade of energy from large scales to small scales, as suggested by from the increase in S_{ww} at frequencies greater than 1 Hz for the irregular ripples (Figure 6). A second possible mechanism is production at small scales in the shear layer and reattachment zone surrounding the recirculation region in the lee of a ripple crest, as suggested by laboratory studies of vertical turbulence intensities in unidirectional flow over dunes [*Bennett and Best*, 1995].

[56] For the cross ripple case, the wave phase averages of suspended sediment concentration and suspended sediment fluxes indicate a vortex shedding process where a vortex is shed immediately after the zero up crossing. A diffusive wave phase signature (an enhancement in turbulence intensity and suspended sediment concentration just before wave phase reversal) is not found for the cross ripples. Similarly, a diffusive signature is not found in the wave phase averages of the turbulence intensity or

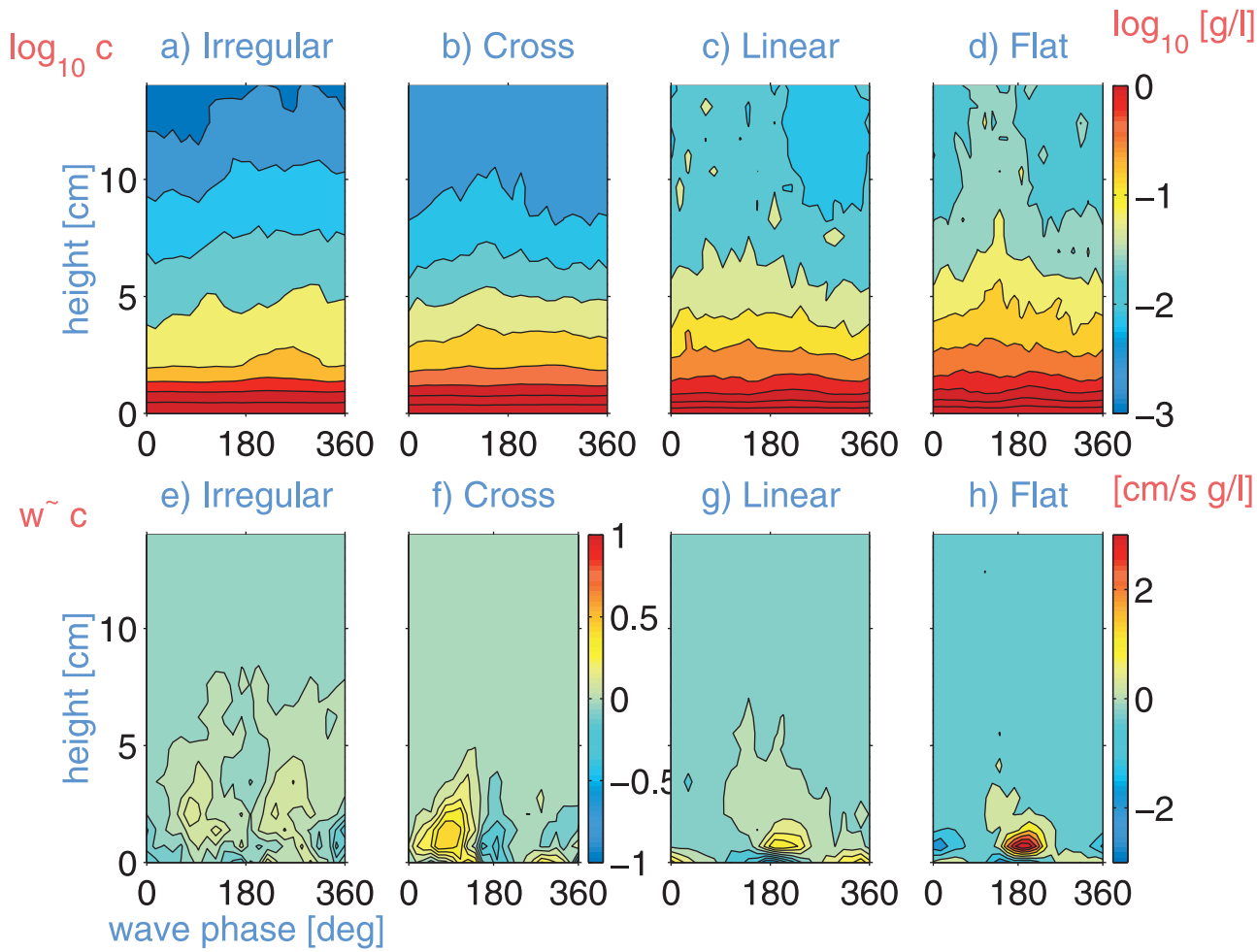

Figure 11. (a)–(d) Wave phase averages of the logarithm of the suspended sediment concentration (including the mean) for the four bed states. (e)–(h) Wave phase averages of the low-frequency vertical flux. Same data sets as in the previous figure. Note that Figures 11e and 11f have a different color scale than Figures 10g and 10h.

suspended sediment concentration for the high-energy cases.

7. Discussion and Comparison to Model Predictions

[57] In this section, the predictions of the friction velocity from different models are compared to the measured vertical turbulence intensity. Since the models were developed from fluid turbulence measurements, it is important at this stage to determine the level of consistency between fluid phase and particle phase estimates of turbulence intensity.

7.1. Fluid Versus Particle Turbulence Intensity

[58] If sand particles are passive tracers of the fluid, then turbulence estimates for the two phases are the same. The CDP is capable of measuring the velocity of very fine particles, as demonstrated by Figure 2. In Figure 2, wave velocities above the near-bed suspension layer are of high quality (average correlation coefficient >0.9), even though the backscatter amplitude is small, implying that there are fine particles present. Thus the measured CDP velocities are associated with both fine and sand-sized particles, but are likely dominated by sand grain velocities close to the bed.

[59] Because of their inertia, particles cannot completely follow the high frequency fluctuations of the turbulence [*Yudine*, 1959; *Siegel and Plueddeman*, 1991]. Also, due to settling, particles fall through turbulent structures so that heavy particles tend to lose velocity correlation more rapidly than light particles of the same size and therefore disperse less: the crossing trajectories effect [*Yudine*, 1959; *Csanady*, 1963].

[60] *Siegel and Plueddeman* [1991] modeled the response of a solid sphere with Stokes drag and found that quartz spheres move with the fluid if the oscillation frequency is less than a critical value, f_c. The time constant associated with this critical value is approximately

$$\tau_c = \frac{1}{f_c} = \frac{10a^2}{\nu,} \tag{25}$$

where a is the particle radius and ν is the kinematic viscosity of the fluid. Choosing a particle radius of 87.5 μm consistent with the sediment samples, this critical frequency is 13 Hz, close to the Nyquist frequency of the field measurements.

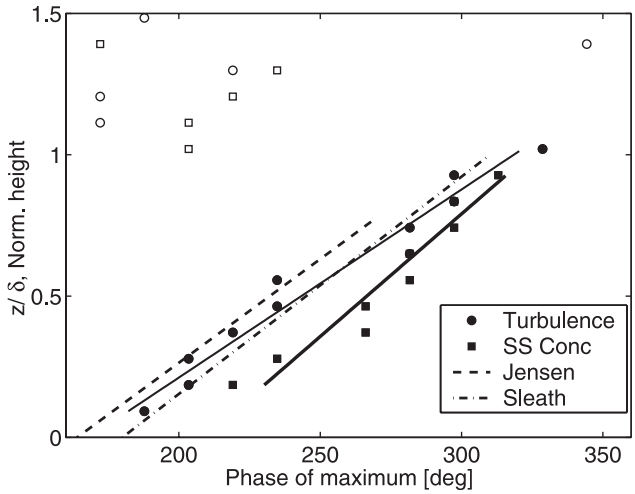

Figure 12. Upward propagation velocities estimated from the wave phase averages of turbulence RMS velocity (circles) and suspended sediment concentration (squares) for irregular ripples. Also shown is the slope of 0.44 from *Sleath* [1987], and an estimated slope of 0.42 from data from *Jensen et al.* [1989] for run 12. This wave flume run over fixed sand had a horizontal wave velocity of 1 m/s, and a period of 9.72 s. Data included in the calculation of the slope are indicated by filled symbols.

This result suggests that the measured particle turbulence intensities would approximately equal the fluid turbulence intensities. However, a Stokes drag is inaccurate for the sand particles in this experiment as the particle Reynolds number is approximately 3.5. For larger particles, *Snyder and Lumley* [1971] gave a generalized time constant:

$$\tau_p = \overline{w}_s/g, \tag{26}$$

where $\bar{w}_s$ is the still water particle settling velocity and g is the acceleration due to gravity For a Stokes quartz particle this becomes $\tau_p = 0.4\frac{a^2}{\nu}$, and has the same form as equation (25).

[61] In a laboratory study by *Wells and Stock* [1983] using grid-generated turbulence, the effects of crossing trajectories and particle inertia on the turbulent energy decay were isolated. The crossing trajectories effect did not significantly change the rate of turbulence decay. Particle inertia effects were estimated by using two sizes of glass beads. For particles with d_{50} = 5 μm, the turbulent energy decay was identical to that of the fluid. However, the turbulent energy of the 57 μm particles was found to be approximately 30% lower than that of the fluid. The ratio of the particle time constant to the Kolmogorov timescale was found to be a good indicator of the effects of particle inertia. The Kolmogorov timescale is

$$\tau_k = \left(\frac{\nu}{\epsilon}\right)^{1/2}, \tag{27}$$

where ν is the kinematic viscosity of the fluid and ϵ is the rate of dissipation of turbulent energy. In the *Wells and Stock* [1983] experiment, the ratios of τ_p/τ_k were 0.024 and 2.97. In a vertical wind tunnel experiment with grid-generated turbulence, *Snyder and Lumley* [1971] found that due to particle inertia the turbulence intensity was smaller than the fluid for particles with timescale ratios of 1.72, 3.85, and 4.21. The authors also included particles with a timescale ratio of 0.145, and expected the particles to follow the flow but found lower turbulence estimates due to measurement difficulties.

[62] In the present study the still water settling velocity was determined by measuring the settling velocity of individual particles from sieved sand samples (125–455 μm in 0.25ϕ intervals). Settling velocities for size fractions smaller than 125 μ m were estimated using a Stokes drag law. The average settling velocity weighted by the size distribution was 2 cm/s. Substituting this value in equation (26) gives a particle time constant of 2 ms. The dissipation rate maximum is 9.3 cm^2/s^3 (section 4.4), which gives a minimum Kolmogorov timescale of 33 ms. Thus, the measured maximum timescale ratio is 0.06, larger than the timescale ratio for the smaller particles in the *Wells and Stock* [1983] experiment (0.024) and smaller than the timescale ratio forthe smallest particles in the *Snyder and Lumley* [1971] experiment (0.145). Their results therefore suggest that the sand-size particle turbulence intensity should approximately equal that of the fluid turbulence in the present measurements. However, given the measurement difficulties in the *Snyder and Lumley* [1971] experiment and the differences between intermittent wave boundary layer turbulence and grid turbulence, this conclusion is tentative and further investigation is warranted.

7.2. Bed Stress Model Predictions

[63] Figure 13 shows the measured peak near-bed significant vertical turbulence intensity and the friction velocity estimates for the bed stress model. It is assumed the friction velocity is twice the significant vertical turbulence intensity (section 2.1).

[64] The trend of the model predictions using a grain roughness friction factor [*Swart*, 1974] is inconsistent with the trend of the measured values, as the predicted friction velocities increase with wave energy, whereas the measured values first decrease, then increase. Friction velocities predicted using friction factors by *Tolman* [1994] include a parameterized ripple roughness and are consistent with the measurements, both trend and magnitude.

[65] Figure 14 presents the observed wave friction factor estimated from the horizontal wave orbital RMS velocity:

$$f_w = 2\left(\frac{2w'_{1/3}}{u_{1/3}}\right)^2, \tag{28}$$

where the friction velocity, u_*, is assumed to be twice the peak significant vertical turbulence intensity. Observed values are plotted relative to grain roughness Shields parameter, θ_d calculated using the skin friction for the friction factor ($k_N = D$ in equation (2)), rather than $\theta_{2.5}$ in order to facilitate comparison to *Tolman* [1994]. Two estimates are given as both methods of velocity decomposition were used to estimate the turbulence intensity. Also shown in this Figure are the predicted wave friction factors from *Swart* [1974] and *Nielsen* [1992], *Tolman* [1994], and *Grant and Madsen* [1982]. Wave Friction factors predicted by *Grant and*

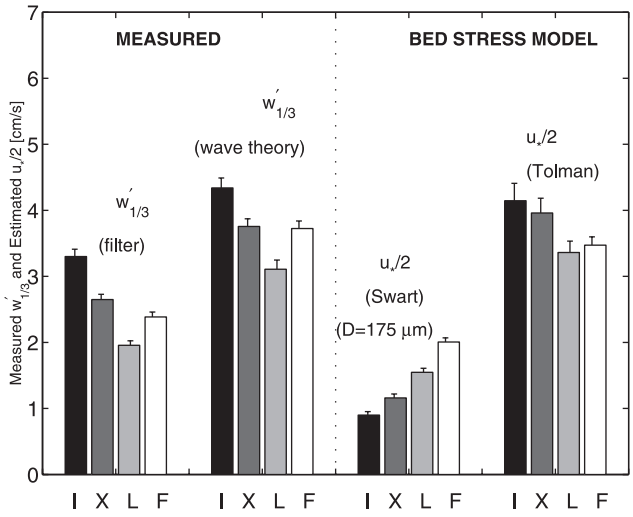

Figure 13. Measured values of the maximum significant turbulence intensity, $w'_{1/3}$ in comparison with friction velocities predicted using the bed stress model. Each measurement or prediction contains the four bed states: I = Irregular ripples; X = Cross Ripples; L = Linear transition ripples; and F = Flat bed. Error bars identify the standard deviation about the mean, with 61, 77, 10, and 12 data sets for the four bed states. Data for which the maximum in turbulence intensity was at 0 cm or above 5.3 cm were not included.

Madsen [1982] generally overestimate the measured values, but those by *Tolman* [1994] are generally consistent with the measurements. Predictions from *Swart* [1974] and *Nielsen* [1992] are generally constant for all bed states, a trend which is inconsistent with the measurements. Wave friction factors from *Swart* [1974] (equation (6)) were modified by *Nielsen* [1992, p. 158] to include ripple roughness and a contribution from moving grains in the roughness parameter (equation (7)). For flat bed conditions $8\eta^2/\lambda$ is replaced by a grain roughness 2 d_{50}. Equation (7) is based on observations from *Carstens et al.* [1969], a laboratory study in an oscillatory water tunnel with a mobile bed, fixed oscillation period and a range of oscillation amplitudes. Measurements of the additional energy dissipation relative to a smooth bed were determined from measurements of work input into the water tunnel. Using the observed energy dissipation factors, *Nielsen* [1992, p. 153] found the bed roughness by inverting the friction factor formula from *Swart* [1974] (equation (6)), and estimating the roughness in terms of ripple height and wavelength, giving equation (7). Equation (6) is likely the reason why the predictions underestimate the wave friction factors for rippled beds as this relation was derived from laboratory measurements of fixed grain roughness and monochromatic waves. In addition, the ripple steepness tends to be smaller for field conditions (irregular waves) [*Nielsen*, 1992, p. 140], which would result in a smaller predicted wave friction factor.

[66] *Grant and Madsen* [1982] show that the wave-induced roughness, $k_N = k_r + k_s$, is the sum of a ripple-induced roughness, k_r, and a sheet flow roughness, k_s. *Tolman* [1994] also uses a combined roughness, but replaces the ripple roughness and sheet flow roughness with more recent empirical relations. The ripple roughness by *Grant and Madsen* [1982] was based on observations for monochromatic waves. However, results from *Madsen et al.* [1990] indicate that irregular waves result in a hydrodynamically smoother bottom than monochromatic waves for identical ripple heights and steepnesses. Thus *Tolman* [1994] uses the empirical relation of *Madsen et al.* [1990] for ripple roughness:

$$k_r = 1.5A\frac{\theta_d}{\theta_c}^{-2.5}, \tag{29}$$

where θ_d is the grain roughness Shields parameter calculated using the grain diameter, and θ_c, the critical Shields parameter below which no sediment motion occurs. For the above estimates of f_w, a critical grain roughness Shields parameter of 0.067 was selected. The sheet flow roughness, k_s in *Grant and Madsen* [1982] overestimates the roughness according to *Wiberg and Rubin* [1989], and was replaced in Tolman's model by an empirical relation from *Wilson* [1989], where

$$k_s = 0.0655A\left(\frac{u_{1/3}^2}{(s-1)gA}\right)^{1.4}. \tag{30}$$

[67] Clearly, the more recent roughness parameterizations improve the predictions of the measured friction factors, although for linear transition ripples the roughness appears to be somewhat too large. Measured and estimated wave friction factors for the four bed states are given in Table 2.

7.3. Sediment Eddy Diffusion Model Predictions

[68] The sediment eddy diffusion model is based on an assumed vertical flux balance and parameterizes the turbu-

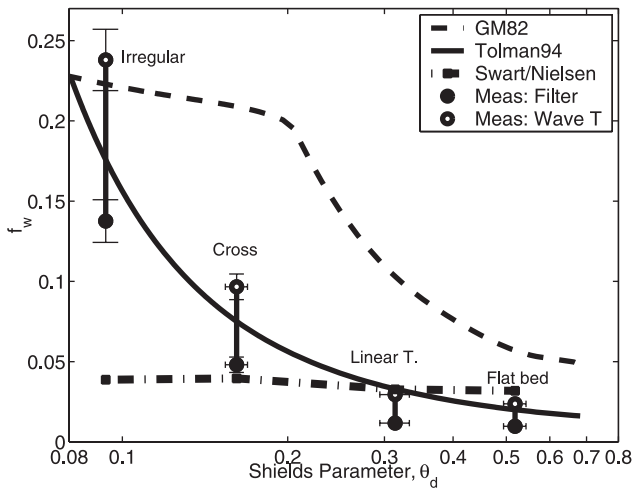

Figure 14. Measured values of wave friction factor in comparison with predicted friction factors (equation (5)) as a function of grain roughness Shields parameter. For each bed state, the symbols indicate the measured values from the linear wave theory decomposition method (open symbols) and the filter velocity decomposition method (filled symbols). Also shown are the predicted wave friction factors from *Swart* [1974] and *Nielsen* [1992] (plus symbols), *Tolman* [1994] (solid line), and *Grant and Madsen* [1982] (dashed line).

Table 2. Measured and Estimated Wave Friction Factors for the Four Bed States[a]

	Irregular	Cross	Linear	Flat
f_w (filter)	0.14	0.048	0.012	0.0097
f_w (LWT)	0.24	0.1	0.03	0.024
u_{20}, cm/s	25	34	51	68
u_*, cm/s	5.6	4.6	3.5	4.3
δ, cm	7.4	6.3	4.8	6.0
h, m	3.2	3.2	3.1	3.7

[a] Some experiment summary information is also given, including significant horizontal velocity u_{20}, friction velocity, u_*, boundary layer thickness, δ, and average water depth, h.

lent sediment flux by a sediment eddy diffusivity, K, times the mean concentration gradient (equation (13)). The sediment eddy diffusivity is assumed to have a linear region near the bed.

[69] Figure 15 shows estimates of K from the measurements, equation (13). As the high frequency (>2 Hz) suspended sediment fluxes are small, the estimates of the sediment eddy diffusivity are very small when the filter method is used. A linear region is found near the bed for the linear wave theory decomposition method except in the case of irregular ripples. Regression correlation coefficients for the other bed states are greater than 0.9 for the linear wave theory method, but are lower for the filter method ($r^2 > 0.7$). In the case of the irregular ripples, the assumption of a vertical flux balance is not valid, as shown in section 5. Overall, the magnitude of the sediment eddy diffusivity is much smaller than estimates from measurements of the peak significant turbulence intensity, which are also shown in Figure 15.

[70] The estimates of u_* converted from slope of the eddy diffusivity are 0.52, 0.76 and 0.86 cm/s for cross ripples, linear transition ripples and flat bed, respectively. These values are approximately 20% of the measured values of the maximum significant vertical turbulence intensity for the linear wave theory method, suggesting the ratio of the sediment eddy diffusivity to the eddy viscosity is approximately 0.2.

7.4. Vortex Shedding Model Predictions

[71] For the vortex shedding model, the measured values of b_s (equation (14)), were determined by fitting the slope of $1/w'_{1/3}$ to z. Only the portion of the profile above the turbulence intensity maximum is used in the linear fit, over at least 4 points, with a restriction on the regression correlation coefficient ($r^2 > 0.8$). Using three estimates of bed roughness (η, λ, r) the predictions of b_s are closest to the measured values for irregular and linear transition ripples when the ripple wavelength is used (Figure 16). For flat bed, the predictions of b_s are all too high.

[72] In a similar investigation in a wave flume, *Zedel and Hay* [1998] found that for low energies, the value of b_s (calculated using the ripple wavelength) was larger than the observations by a factor of 3, indicating that at any given height the turbulence intensities are larger than the values expected from the grid turbulence model.

8. Summary and Conclusions

[73] In this study, field measurements of near-bed turbulence and suspended sediment fluxes were compared for a variety of bed states. Simultaneous vertical and horizontal profiles of particle velocity and suspended sediment concentration were collected using a dual-beam Coherent Doppler Profiler over an 11 day field experiment. Bed form dimensions, bed slopes and bed form type were obtained using rotary sonars for four distinct bed states (irregular ripples, cross ripples, linear transition ripples, and flat bed) during low energy waves, storm and long period swell

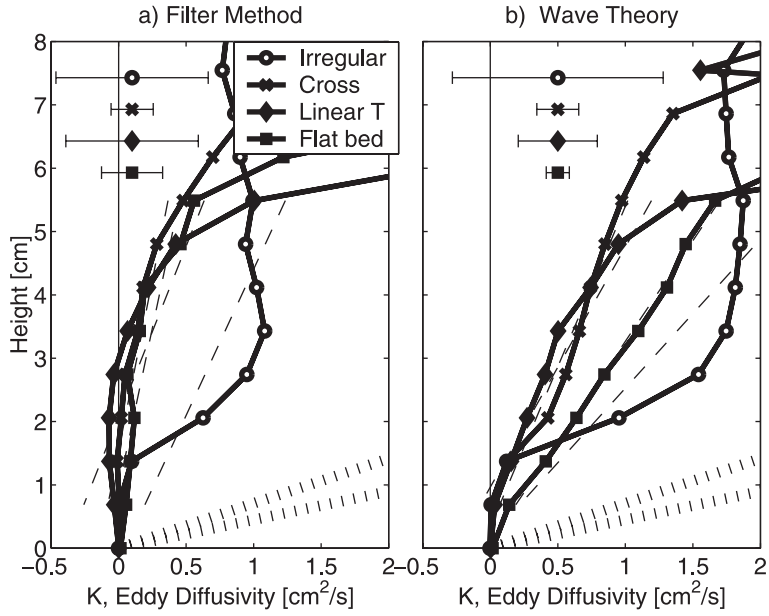

Figure 15. Estimates of the sediment eddy diffusivity, K as a function of height. The dashed lines indicate linear fits for each bed state. The dotted lines indicate the range of sediment eddy diffusivities estimated from the measured turbulence intensity. Confidence intervals (80%) estimated at z = 4 cm are indicated in the upper left-hand corner.

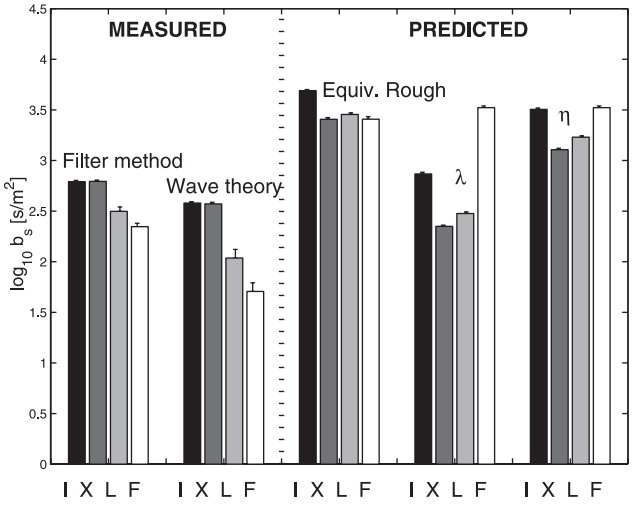

Figure 16. A comparison of measured slopes of $1/w'_{1/3}$ versus height and the predictions from Sleath's model. Model predictions used three estimates of bed roughness: equivalent roughness, η, ripple height, λ, and ripple wavelength. Error bars identify the standard error about the mean. Number of data sets included: Filter method: Irregular 59, Cross 73, Linear Transition 13, and Flat 12. Linear wave theory method: Irregular 59, Cross 67, Linear Transition 11, and Flat Bed 13.

conditions. The objective was to quantify the characteristics of near-bed turbulence and suspended sediment fluxes as a function of bed state by comparing profiles of time-averaged and wave phase averaged quantities, determining the upward propagation velocity, and to compare measured peak turbulence intensities to model predictions. A secondary objective was to determine if the observations matched a vortex shedding process or a diffusion process based on laboratory observations of these mechanisms.

[74] Three different methods were selected to separate the turbulent component of the velocity from the mean and wave components, including a filter method, an inviscid linear wave theory method, and a dissipation rate method. Predicted turbulence levels are expected to be underestimated by the filter method and overestimated by the linear wave theory method. These two methods predict near-bed turbulence intensities within a factor of $1-2$ of each other, which suggests that the actual turbulence intensity is well constrained. The dissipation rate method gives lower estimates of turbulence intensity for all bed states. This model assumes a $-5/3$ slope in the inertial subrange that is generally not found in near-bed measurements. The absence of a $-5/3$ slope suggests large scale turbulence is suppressed near the bed, and that the inertial subrange is narrow.

[75] Profiles of turbulence intensity for the low-energy cases have a peak at 2 cm above the bed and then fall off slowly with height. For the high-energy cases, the near-bed turbulence intensities are nearly constant with height. Near-bed values of turbulence intensity are approximately the same for the four bed states even though the wave energies are very different. Measurements were compared to predictions of the friction velocity using a bed stress model, and an eddy diffusion model. The bed stress model predictions of the friction velocity were estimated with three parameterizations of the wave friction factor. The best predictions were based on the wave friction factors given in *Tolman* [1994]. Predictions of the friction velocity based on the sediment eddy diffusion model are approximately 20% of the measured peak in significant turbulence intensity. The discrepancy is due in part to the formulation of the sediment eddy diffusivity as the data show that the sediment eddy diffusivity only increases linearly with height when the wave component of the suspended sediment flux is small. The rate of turbulence decay with height was predicted by a grid-stirring model [*Sleath*, 1987] and compared to the observations. This model generally underpredicts the level of turbulence at each height for all bed states. The closest predictions were found when the ripple wavelength was used for the roughness parameterization.

[76] Profiles of vertical suspended sediment fluxes show that in general, there is a balance between downward settling due to gravity and upward fluxes due to vertical velocity fluctuations within the incident wave band, including low-frequency turbulence. Exceptions to this balance are found very close to the bed, and for the irregular ripple case, when the ripples did not migrate. The suspended sediment flux contribution associated with the high-frequency vertical velocity fluctuations is small. Normalized suspended sediment flux cospectra have a small, but significant peak at incident wave frequencies for all bed states that is constant throughout the boundary layer.

[77] Wave phase averages of turbulence intensity, suspended sediment concentration and suspended sediment fluxes were examined for either vortex shedding or diffusion signatures. The irregular ripples show strong signatures in the wave phase averaged quantities, revealing an upward propagation of turbulence and suspended sediment away from the bed just after the peak onshore flow. Estimated upward propagation velocities from the turbulence intensity and the suspended sediment concentration overlap the upward propagation velocities measured from laboratory experiments over fixed grain roughness. For cross ripples, the wave phase averages have a weak signature of vortex shedding, but no evidence of diffusion. For the high-energy cases, the wave phase averaged velocity indicates the vertical velocity at the bed is induced by the waves flowing over a sloped surface. The wave phase averaged suspended sediment concentration does not exhibit a diffusive signature.

Appendix A: Determining of Seafloor Elevation From Acoustic Backscatter

[78] Possible means of determining the seafloor elevation automatically with subcentimeter resolution during active sediment transport conditions include finding concentrations on the order of the seafloor sediment concentration (>1000 g/L), or identifying the location of stationary sediments. These methods are not suitable for the CDP as the maximum measured sediment concentrations are far below the seafloor sediment concentration, and noise in the velocity data obscures the zero velocity at the seafloor. The

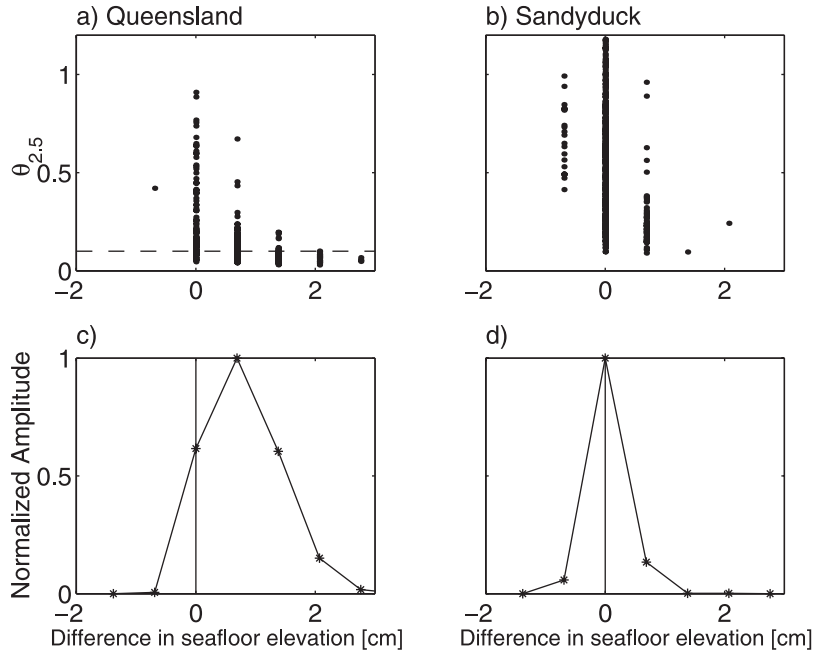

Figure A1. Grain roughness Shields parameter versus the difference of the seafloor elevation estimates for (a) Queensland, and (b) Duck data. (c) and (d) Normalized histograms of the difference in seafloor elevation estimates. Data from Queensland Beach, Nova Scotia, includes 412, 7 min data files. Data from SandyDuck97, North Carolina, includes 615, 20–25 min. data files.

objective of this Section is to test and compare two methods of identifying the seafloor elevation. The first method considered is based on the 50th percentile of the suspended sediment concentration while the second is based on the velocity RMS gradient.

[79] Often there are four separate layers included in the description of the sediment. A suspension layer is highest up from the bed, and in this layer the sediment motion is strongly influenced by fluid motions. A bed load layer exists close to the bed. In this layer sediments move individually with projectile trajectories, often in response to particle collisions. A sheet flow layer may exist for high wave energies when the upper part of the bed is fluidized and moves as a unit with suspended sediment concentrations on the order of 100 g/L [*Ribberink and Al-Salem*, 1994]. The last layer is the stationary seafloor with a high sediment concentration.

[80] In the first method, the seafloor elevation was selected by determining the location of the 50th percentile of the concentration with a further restriction that the suspended sediment concentration in the range bin above this level be less than 10 g/L. This selection excludes sheet flow and/or bed load layers from the analysis, but the thicknesses of these layers is on the order of the resolution of the instrument. The position of the seafloor from this method was compared to the results of the second method: finding the maximum gradient in the RMS vertical velocity profile.

[81] Two data sets were included in this analysis. For the data from Queensland Beach, the seafloor elevation was determined using the above two methods using averages of approximately 30 s of data. The final estimate of the seafloor elevation for each data file was taken as the median of these values. A similar procedure was followed for the second data set which was collected during SandyDuck97, North Carolina. This data set had longer time series (20–25 min), so the data record was split into approximately 1 min sections. Figure A1 shows the seafloor elevation found by the velocity RMS method minus the seafloor elevation found by the 50th percentile method.

[82] For the Queensland Beach data, the difference in seafloor elevation is positively correlated with grain roughness Shields parameter. The normalized histogram of the difference is centered at 0.69 cm, or 1 range bin. In contrast, the second data set from SandyDuck97, North Carolina, finds the two methods are consistent. According to underwater video images recorded at Queensland, there was a layer of seaweed present during low amplitude wave conditions. The seaweed layer was unattached, and may have caused damping in the velocity close to the bed. In order to avoid any possible effects the seaweed may have on sediment dynamics, a high threshold of $\theta_{2.5} > 0.1$. was used in this comparison. In summary, the two methods of determining the seafloor elevation compare favourably, giving confidence in the 50th percentile method used for the seafloor elevation estimate.

[83] **Acknowledgments.** The authors thank the staff and students of Memorial University and Dalhousie University who were involved in data collection for the Queensland Beach experiment. We would also like to thank R. Craig for developing the data collection software, T. Mudge for processing the rotary sonar images, W. Paul for building the CDP control hardware. This work was funded by the U.S. Office of Naval Research, Coastal Sciences Program, and the Natural Sciences and Engineering Research Council of Canada.

References

Bennett, S. J., and J. L. Best, Mean flow and turbulence structure over fixed, two-dimensional dunes: Implications for sediment transport and bedform stability, *Sedimentology*, *42*, 1995.

Carstens, M. R, F. M. Nielsen, and H. D. Altinbilek, Bedforms generated in the laboratory under an oscillatory flow, *Tech. Rep. 28*, Coastal Eng. Res. Cent., Vicksburg, Miss., 1969.

Clifton, H., Wave-formed sedimentary structures—A conceptual model, in *Beach and Nearshore Sedimentation, SEPM Spec. Publ.*, edited by R. Davis and R. Ethington, vol. 24, pp. 126–148, Soc. for Sediment. Geol., Tulsa, Okla., 1976.

Crawford, A. M., and A. E. Hay, Linear transition ripple migration and wave orbital velocity skewness: Observations, *J. Geophys. Res.*, *106*, 14,113–14,128, 2001.

Csanady, G. T., Turbulent diffusion of heavy particles in the atmosphere, *J. Atmos. Sci.*, *20*, 201–208, 1963.

Davies, A. G., Wave interactions with rippled sand beds, *Physical Oceanography of Coastal and Shelf Seas*, chap. 1, pp. 1–62, Elsevier Sci., New York, 1983.

Dyer, K. R., and R. L. Soulsby, Sand transport on the continental shelf, *Ann. Fluid Dyn.*, *20*, 295–324, 1988.

Foster, D. L., Dynamics of the nearshore wave bottom boundary layer, Ph.D. thesis, Oreg. State Univ., Corvallis, 1997.

George, R., R. E. Flick, and R. T. Guza, Observations of turbulence in the surf zone, *J. Geophys. Res.*, *99*, 801–810, 1994.

Glenn, S. M., and W. D. Grant, A suspended sediment stratification correction for combined wave and current flows, *J. Geophys. Res.*, *92*, 8244–8264, 1987.

Grant, W. D., and O. S. Madsen, Combined wave and current interaction with a rough bottom, *J. Geophys. Res.*, *84*, 1797–1808, 1979.

Grant, W. D., and O. S. Madsen, Movable bed roughness in unsteady oscillatory flow, *J. Geophys. Res.*, *87*, 469–481, 1982.

Hay, A. E., Sound scattering from a particle-laden jet, *J. Acoust. Soc. Am.*, *90*, 2055–2074, 1991.

Hay, A. E., and D. J. Wilson, Rotary sidescan images of nearshore bedform evolution during a storm, *Mar. Geol.*, *119*, 57–64, 1994.

Hay, A. E., C. Smyth, L. Zedel, and T. Mudge, On remotely probing the structure of the bottom boundary layer over an evolving sea bed, in Coastal Ocean Processes Symposium: A Tribute to William D. Grant, Woods Hole Oceanogr. Inst. Tech. Rep. WHOI-99-04, pp. 99–106, Woods Hole Oceanogr. Inst., Woods Hole, Mass., 1999.

Hino, M., M. Kashiwayanagi, A. Nakayama, and T. Hara, Experiments on the turbulence statistics and the structure of a reciprocating oscillatory flow, *J. Fluid Mech.*, *131*, 363–400, 1983.

Hinze, J. O., *Turbulence*, McGraw-Hill, New York, 1975.

Jensen, B. L., B. M. Sumer, and J. Fredsoe, Turbulent oscillatory boundary layers at high Reynolds numbers, *J. Fluid Mech.*, *206*, 265–297, 1989.

Jonsson, I. G., Wave boundary layers and friction factors, paper presented at 10th International Conference on Coastal Engineering, Am. Soc. of Civ. Eng., Tokyo, Japan, 1966.

Kosyan, R. D., H. Kunz, S. Y. Kuznetsov, and M. V. Krylenko, Sand suspension events and intermittency of turbulence in the surf zone, paper presented at 26th International Conference on Coastal Engineering, Am. Soc. of Civ. Eng., Copenhagen, Denmark, 1996.

Madsen, O. S., P. P. Mathiesen, and M. M. Rosengaus, Movable bed friction factors for spectral waves, paper presented at 22nd International Conference on Coastal Engineering, Am Soc. of Civ. Eng., Delft, Neth., 1990.

McComb, W. C., *The Physics of Fluid Turbulence*, Oxford Univ. Press, New York, 1990.

Nakato, T., F. Locker, J. R. Glover, and J. F. Kennedy, Wave entrainment of sediment from rippled beds, *J. Waterw. Port Coastal Ocean Eng.*, *103*, 83–99, 1977.

Ngusaru, A. S., Cross-shore migration of lunate mega-ripples and bedload sediment transport models, Ph.D. thesis, Memorial Univ. of Newfoundland, St. John's, Newfoundland, Can., 2000.

Nielsen, P., *Coastal Bottom Boundary Layers and Sediment Transport*, World Sci., River Edge, N.J., 1992.

Osborne, P. D., and C. E. Vincent, Vertical and horizontal structure in suspended sand concentrations and wave-induced fluxes over bedforms, *Mar. Geol.*, *131*, 195–208, 1996.

Ribberink, J. S., and A. A. Al-Salem, Sediment transport in oscillatory boundary layers in cases of rippled beds and sheet flow, *J. Geophys. Res.*, *99*, 12,707–12,727, 1994.

Sheng, J., and A. E. Hay, Sediment eddy diffusivities in the nearshore zone, from multifrequency acoustic backscatter, *Cont. Shelf Res.*, *15*, 129–147, 1995.

Siegel, D. A., and A. J. Plueddemann, The motion of a solid sphere in an oscillating flow: An evaluation of remotely sensed doppler velocity estimates in the sea, *J. Atmos. Oceanic Technol.*, *8*, 296–303, 1991.

Sleath, J. F. A., Turbulent oscillatory flow over rough beds, *J. Fluid Mech.*, *182*, 369–409, 1987.

Sleath, J. F. A., *Seabed Boundary Layers*, vol. 9, John Wiley, New York, 1990.

Sleath, J. F. A., Velocities and shear stresses in wave-current flows, *J. Geophys. Res.*, *96*, 15,237–15,244, 1991.

Smith, J. D., Modeling of sediment transport on continental shelves, in *Marine Modeling*, edited by E. G. Goldberg, J. J. O'Brien, and J. H. Steele, pp. 539–577, 1977.

Snyder, W. H., and J. L. Lumley, Some measurements of particle velocity autocorrelation function in a turbulent flow, *J. Fluid Mech.*, *48*, 41–71, 1971.

Swart, D. H., Offshore sediment transport and equilibrium beach profiles, *Tech. Rep.131*, Delft Hydraul. Lab., Delft, Neth., 1974.

Tennekes, H., and J. L. Lumley, *A First Course in Turbulence*, MIT Press, Cambridge, Mass., 1972.

Thompson, S. M., and J. S. Turner, Mixing across an interface due to turbulence generated by an oscillating grid, *J. Fluid Mech.*, *67*, 349–368, 1975.

Thornton, E. B., Energetics of breaking waves within the surf zone, *J. Geophys. Res.*, *84*, 4931–4938, 1979.

Thornton, E. B., and R. Guza, Transformation of wave height distribution, *J. Geophys. Res.*, *88*, 5925–5938, 1983.

Tolman, H. L., Wind waves and movable-bed bottom friction, *J. Phys. Oceanogr.*, *24*, 994–1009, 1994.

Wells, M. R., and D. E. Stock, The effects of crossing trajectories on the dispersion of particles in a turbulent flow, *J. Fluid Mech.*, *136*, 31–62, 1983.

Wiberg, P. L., and D. M. Rubin, Bed roughness produced by saltating sediment, *J. Geophys. Res.*, *94*, 5011–5016, 1989.

Wiberg, P., and J. D. Smith, A comparison of field data and theoretical models for wave-current interactions at the bed on the continental shelf, *J. Geophys. Res.*, *95*, 11,591–11,601, 1983.

Wilson, D. J., and A. E. Hay, High resolution sidescan sonar observations of small scale sand bedforms under waves: A comparison of field and laboratory measurements, technical report, Memorial Univ. of Newfoundland, St. John's, Newfoundland, Can., 1995.

Wilson, K. C., Friction of wave-induced sheet flow, *Coastal Eng.*, *12*, 371–379, 1989.

Yudine, M. I., Physical considerations on heavy particle diffusion, *Adv. Geophys.*, *6*, 185–191, 1959.

Zedel, L., and A. E. Hay, Coherent doppler sonar: Sediment flux and turbulent velocities in a wave flume, paper presented at 26th International Conference on Coastal Engineering, Am. Soc. of Civ. Eng., Copenhagen, 1998.

Zedel, L., and A. E. Hay, A Coherent Doppler Profiler for high resolution particle velocimetry in the ocean: Laboratory measurements of turbulence and particle flux, *J. Atmos. Oceanic Technol.*, *16*, 1102–1117, 1999.

Zedel, L., A. E. Hay, R. Cabrera, and A. Lohrmann, Performance of a single beam, pulse-to-pulse Coherent Doppler Profiler, *IEEE J. Oceanic Eng.*, *21*, 290–297, 1996.

A. E. Hay and C. Smyth, Department of Oceanography, Dalhousie University, Halifax, N.S., B3H 4J1 Canada. (csmyth@phys.ocean.dal.ca; alex.hay@dal.ca)

L. Zedel, Department of Physics and Physical Oceanography, Memorial University, St. John's, Newfoundland, A1B 3X7 Canada. (zedel@physics.mun.ca)